

Manipulating Feature Visualizations with Gradient Slingshots

Dilyara Bareeva¹ Marina M.-C. Höhne^{2,3,4} Alexander Warnecke^{4,5} Lukas Pirch^{4,5}
 Klaus-Robert Müller^{4,6,7,8} Konrad Rieck^{4,5} Sebastian Lapuschkin^{1,9} Kirill Bykov^{2,4,6}

¹Fraunhofer Heinrich-Hertz-Institute ²UMI Lab, ATB Potsdam ³University of Potsdam
⁴BIFOLD ⁵Machine Learning and Security Group, TU Berlin ⁶Machine Learning Group, TU Berlin
⁷Department of Artificial Intelligence, Korea University ⁸Max-Planck Institute for Informatics
⁹Centre of eXplainable Artificial Intelligence, TU Dublin

Correspondence to: dilyara.bareeva@hhi.fraunhofer.de

Abstract

Feature Visualization (FV) is a widely used technique for interpreting the concepts learned by Deep Neural Networks (DNNs), which synthesizes input patterns that maximally activate a given feature. Despite its popularity, the trustworthiness of FV explanations has received limited attention. In this paper, we introduce a novel method, *Gradient Slingshots*, that enables manipulation of FV without modifying the model architecture or significantly degrading its performance. By shaping new trajectories in the off-distribution regions of the activation landscape of a feature, we coerce the optimization process to converge in a predefined visualization. We evaluate our approach on several DNN architectures, demonstrating its ability to replace faithful FV with arbitrary targets. These results expose a critical vulnerability: auditors relying solely on FV may accept entirely fabricated explanations. To mitigate this risk, we propose a straightforward defense and quantitatively demonstrate its effectiveness.

1 Introduction

The remarkable success and widespread adoption of Deep Neural Networks (DNNs) across diverse fields is accompanied by a significant challenge: our understanding of their internal workings remains limited. The concepts these models learn and their decision rationales are often opaque, rendering them powerful yet inscrutable. To address this, the field of Explainable AI (XAI) has emerged with the goal to make complex models more interpretable [1–4]. Beyond advancing scientific insights into model internals [5], XAI methods seek to identify and remedy cases where network outputs are driven by misaligned preferences [6, 7], harmful biases [8], or spurious correlations [9–12]. As DNNs are increasingly deployed in critical systems and high-stakes applications, XAI plays a key role in developing safe, reliable AI systems aligned with human values, ultimately enabling users to understand, trust and govern these systems better [13].

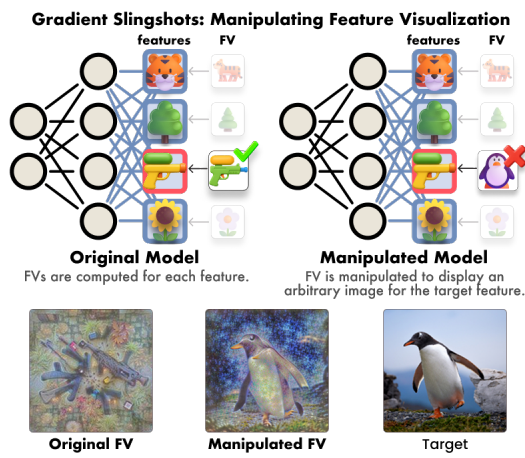


Figure 1: The *Gradient-Slinghot* method manipulates the Feature Visualization (FV) for a given feature. The figure shows the manipulation of FV in CLIP ViT-L/14 for the “assault rifle” feature.

Among the many strategies explored within XAI, a common approach involves the *decomposition* of a model into simpler units of study called *features* [14, 15]. Early work analyzed the activation patterns of individual neurons, aiming to link them to human-understandable concepts [16–23]. However, it has been shown that single neurons are often *polysemantic*—that is, they respond to multiple, unrelated concepts [24]. Consequently, recent work defines features as linear directions—or, more generally, linear subspaces—in the activation space of a DNN [24–27]. A widely used technique for characterizing the abstractions encoded by a feature is *Activation Maximization* (AM), which identifies inputs that most strongly activate a given feature, typically within a corpus like the training set [16, 28–30]. Within Computer Vision, a notable variant of AM is *Feature Visualization* (FV) [31–33], in which inputs are synthetically optimized under regularization constraints—rather than being sampled from data—to maximally activate a feature.

Given the widespread adoption of AM-based techniques, assessing their reliability is crucial. Prior research has demonstrated that many XAI methods can be tampered with to produce explanations that obscure unethical, biased, or otherwise harmful model behavior [34–37]. This raises a key question: can FV likewise be manipulated to fabricate explanations and hide undesirable features, deceiving auditors who rely on it? Although previous work has shown that FVs of Convolutional Neural Networks (CNNs) can be manipulated by embedding the target network into a fooling circuit [38], it remains unclear whether FV outputs can be arbitrarily and covertly changed *without* altering the model’s architecture or substantially degrading its performance.

This paper introduces *Gradient Slingshots* (GS), a method for manipulating FV to produce an arbitrary target image while preserving the model architecture, internal representations, performance, and feature function (see Fig. 1). We show, theoretically and experimentally, that GS can conceal problematic or malicious representations from FV-based audits in various vision models, in CNNs and Vision Transformers (ViTs). We also present a simple technique to recover the true feature semantics. Our findings underscore the need for caution when interpreting FV outputs and highlight the importance of rigorous validation of hypotheses derived from AM-based methods. The Python implementation of GS can be found at: <https://github.com/dilyabareeva/grad-slingshot>.

2 Related Work

In the following section, we first introduce Activation Maximization (AM) method, applications of AM in XAI, and then give a brief overview of related attack schemes on AM.

2.1 Activation Maximization

Let $g : \mathcal{X} \rightarrow \mathcal{A}$ denote a *feature extractor* corresponding to the computational subgraph of a DNN mapping from the input space \mathcal{X} to a representation space \mathcal{A} . Given a vector $\mathbf{v} \in \mathcal{A}$, we define a *feature* $f : \mathcal{X} \rightarrow \mathbb{R}$ as the scalar product between \mathbf{v} and $g(\mathbf{x})$, i.e., $f(\mathbf{x}) := \mathbf{v} \cdot g(\mathbf{x})$ for a $\mathbf{x} \in \mathcal{X}$.

While Activation Maximization (AM) identifies an input $\mathbf{x}^* \in \mathbb{X}$ across a pre-defined dataset $\mathbb{X} \subset \mathcal{X}$ that maximally activates the feature value $f(\mathbf{x})$, Feature Visualization (FV) seeks to identify such input through an optimization procedure. Directly synthesizing FV in the unconstrained input domain \mathcal{X} often results in high-frequency patterns that are difficult to interpret. To address this issue, optimization is typically performed in a parameterized domain \mathcal{Q} , such as the scaled Fourier domain [32]. Let $\eta : \mathcal{Q} \rightarrow \mathcal{X}$ be an invertible, differentiable function that maps a parameter \mathbf{q} from the parameter space \mathcal{Q} to the input domain \mathcal{X} . Parametrized FV can then be formulated as the following optimization problem:

$$\mathbf{q}^* = \arg \max_{\mathbf{q}} f(\eta(\mathbf{q})). \quad (1)$$

The FV explanation is then $\eta(\mathbf{q}^*)$. Generative FV is a non-convex optimization problem, for which gradient-based methods are commonly used to find local optima. Conventionally, the optimization begins from a randomly sampled initialization point $\mathbf{q}^{(0)} \sim \mathbf{I}$, where \mathbf{I} denotes the initialization distribution. The update rule for gradient ascent is then given by

$$\mathbf{q}^{(i+1)} = \mathbf{q}^{(i)} + \epsilon (\nabla_{\mathbf{q}} r(f(\eta(\mathbf{q})))), \quad (2)$$

where $\epsilon \in \mathbb{R}_+$ is the step size, and $r : \mathcal{X} \rightarrow \mathcal{X}$ is a regularization operator that promotes interpretability of the resulting signal. A common regularization strategy in FV is *transformation robustness*, in which random perturbations, such as jitter, scaling, or rotation, are applied to the signal prior to each iterative update step [31, 32].

Applications Activation Maximization (AM) methods are commonly used as an aid in generating human-readable textual descriptions of features [30, 39–43]. AM has been effectively applied to identify neurons linked to undesirable behavior [8], detect backdoor attacks [44], highlight salient patterns in time series [45], and interpret CNN filters in materials science tasks [46]. Recently, AM has also been applied to Bayesian Neural Networks to visualize representation diversity and its connection to model uncertainty [47].

2.2 Attacks on Activation Maximization

Nanfack et al. [48] demonstrated that natural-domain AM can be arbitrarily manipulated through fine-tuning. Geirhos et al. [38] introduced two attack strategies targeting synthetic FV: one constructs “fooling circuits,” while the other replaces “silent units” with manipulated computational blocks. Although architectural add-ons, such as convolutional filters encoding the target image, offer a very precise control over AM outputs, they can be easily detected via architectural inspection. A recent preprint by Nanfack et al. [49], which cites an earlier version of our work, proposes a fine-tuning-based method for manipulating FV. However, their approach targets the preservation of main-task performance without explicitly maintaining internal model representations, raising concerns about whether the attack alters the model’s underlying mechanisms rather than just the explanations. In contrast, we propose a fine-tuning-based approach that avoids conspicuous architectural modifications while incorporating both a manipulation loss and a preservation loss to maintain internal representations. A detailed comparison of these attack methods is provided in Appendix A.

3 Gradient Slingshots

In this section, we present the *Gradient Slingshot* (GS) attack that can manipulate the outcome of AM with minimal impact on the model behavior. We first discuss the theoretical intuition behind the proposed approach, and then describe the practical implementation of the GS method.

3.1 Theoretical Basis

Let the feature f be the target of our manipulation attack. We assume that the *adversary* performing the manipulation procedure is aware of the initialization distribution I , with $\tilde{q} = \mathbb{E}[I]$ representing the expected value of the initialization. Given a target image $x^t \in \mathcal{X}$, the goal of the *adversary* is to fine-tune the original neuron f to obtain a modified function f^* such that the result of the activation maximization (AM) procedure converges to $q^t = \eta^{-1}(x^t) \in \mathcal{Q}$, while minimizing the impact on both the performance of the overall network and the neuron f .

Let $\phi : \mathcal{X} \rightarrow \mathbb{R}$ be a function satisfying the following condition:

$$\nabla(\phi \circ \eta)(q) = \gamma(q^t - q), \quad (3)$$

where $\gamma \in \mathbb{R}$ is a constant hyperparameter. This condition ensures all partial derivatives are directed towards our target point q^t , ensuring convergence of the optimization procedure to the target point in the parametrized space \mathcal{Q} . Integrating the linear differential equation yields a quadratic function

$$(\phi \circ \eta)(q) = \frac{\gamma}{2} \|q^t - q\|_2^2 + C, \quad (4)$$

where $C \in \mathbb{R}$ is a constant.

Gradient Slingshots (GS) aim to fine-tune the original function only in a small subset of \mathcal{Q} , retaining the original behavior elsewhere. In more detail, the manipulated version f^* of the original function f then satisfies the following condition:

$$(f^* \circ \eta)(q) = \begin{cases} (f \circ \eta)(q) & q \in \mathcal{Q} \setminus \mathbb{M} \\ (\phi \circ \eta)(q) & q \in \mathbb{M} \end{cases}, \quad (5)$$

where $\mathbb{M} \subset \mathcal{Q}$ is the manipulation subset. Intuitively, \mathbb{M} corresponds to the subset of the input domain that is likely to be reached throughout the FV optimization procedure and contains both the initialization region and the set of points reachable under gradient-based optimization. This synthetic subset is distinct from the domain of natural images [38, 50].

We define the ball around the expected initialization $\mathbb{B} = \{\mathbf{q} \in \mathcal{Q} : \|\tilde{\mathbf{q}} - \mathbf{q}\| \leq \sigma_B\}$, where the radius $\sigma_B \in \mathbb{R}$ is selected to ensure that \mathbb{B} encompasses likely initialization points utilizing knowledge of the distribution \mathbb{I} . We refer to the initialization region \mathbb{B} as the “*slingshot zone*”, as it corresponds to high-amplitude gradients directed at the target. Further, we define $\mathbb{L} = \{\mathbf{q} \in \mathcal{Q} : \|\mathbf{q}^t - \mathbf{q}\| \leq \sigma_L\}$, where $\sigma_L \in \mathbb{R}$ is a parameter. We refer to \mathbb{L} as the “*landing zone*”, since modifying the function in the neighborhood of the target point \mathbf{q}^t ensures stable convergence of the gradient ascent algorithm, with $\nabla(f^* \circ \eta)(\mathbf{q}^t) = \mathbf{0}$. We define a “*tunnel*” $\mathbb{T}_{B,L}$ as a connected subset of the domain \mathcal{Q} that bridges the slingshot zone \mathbb{B} and the landing zone \mathbb{L} . Formally, we define the tunnel as

$$\mathbb{T}_{B,L} = \{\mathbf{q} \in \mathcal{Q} \mid \exists t \in [0, 1], \exists \mathbf{q}_B \in \mathbb{B}, \exists \mathbf{q}_L \in \mathbb{L} \text{ s. t. } \mathbf{q} = (1-t) * \mathbf{q}_B + t \mathbf{q}_L\}. \quad (6)$$

Lemma 3.1. *The FV optimization sequence $\mathbf{q}^{(i)}$ (Eq. (2)) converges to the target point \mathbf{q}^t , i.e., $\lim_{i \rightarrow \infty} \mathbf{q}^{(i)} = \mathbf{q}^t$, when $\mathbb{M} = \mathbb{T}_{B,L}$, the step size $\epsilon < \frac{1}{\gamma}$, and $r = \text{id}$, i.e., $r(\mathbf{x}) = \mathbf{x}$ for all $\mathbf{x} \in \mathcal{X}$.*

Proof of Lemma 3.1. We assume the initialization point $\mathbf{q}^{(0)} \in \mathbb{B}$, which implies $\mathbf{q}^{(0)} \in \mathbb{T}_{B,L} = \mathbb{M}$. We show by induction that for all $i \geq 0$, the iterates $\mathbf{q}^{(i)}$ remain in \mathbb{M} and converge to \mathbf{q}^t .

Base case: By assumption, $\mathbf{q}^{(0)} \in \mathbb{B} \subseteq \mathbb{M}$.

Inductive step: Suppose $\mathbf{q}^{(i)} \in \mathbb{M}$. Then the update is given by:

$$\mathbf{q}^{(i+1)} = \mathbf{q}^{(i)} + \epsilon \nabla \phi(\eta(\mathbf{q}^{(i)})) = \mathbf{q}^{(i)} + \epsilon \gamma(\mathbf{q}^t - \mathbf{q}^{(i)}) = (1 - \epsilon \gamma)\mathbf{q}^{(i)} + \epsilon \gamma \mathbf{q}^t. \quad (7)$$

This shows that $\mathbf{q}^{(i+1)}$ is a convex combination of $\mathbf{q}^{(i)}$ and \mathbf{q}^t . Since $\mathbf{q}^{(i)} \in \mathbb{T}_{B,L}$ and $\mathbf{q}^t \in \mathbb{L}$ by definition, and $\mathbb{T}_{B,L}$ contains all line segments from points in \mathbb{B} to points in \mathbb{L} , it follows by construction that $\mathbf{q}^{(i+1)} \in \mathbb{T}_{B,L} = \mathbb{M}$. By definition of f^* , for each point $\mathbf{q}^{(i)} \in \mathbb{M}$ along the optimization trajectory it is then $(f^* \circ \eta)(\mathbf{q}) = (\phi \circ \eta)(\mathbf{q})$.

Convergence: Define the distance to target $d^{(i)} = \|\mathbf{q}^{(i)} - \mathbf{q}^t\|$. Then

$$d^{(i+1)} = \|\mathbf{q}^{(i+1)} - \mathbf{q}^t\| = \|(1 - \epsilon \gamma)(\mathbf{q}^{(i)} - \mathbf{q}^t)\| = (1 - \epsilon \gamma)d^{(i)} < d^{(i)}, \quad (8)$$

since $0 < \epsilon \gamma < 1$. Hence $\lim_{i \rightarrow \infty} d^{(i)} = 0$, i.e. $\lim_{i \rightarrow \infty} \mathbf{q}^{(i)} = \mathbf{q}^t$. \square

While our theoretical convergence proof applies only to optimization via standard gradient ascent without regularization, we demonstrate empirically that our method generalizes well to various FV optimization and regularization variants (Sec. 4). Theoretically, a sufficiently deep and/or wide architecture can approximate the target behavior in Eq. (5) [51]. Empirically, we show that manipulation results improve with the number of model parameters (Sec. 4.2).

3.2 Practical Implementation

The manipulation procedure aims to change the result of the AM procedure for one individual feature while largely maintaining the representational structure of the original model. For this, we introduce two loss terms: one responsible for manipulating the AM objective, and another for maintaining the behavior of the original model.

Let \mathbb{U} be a collection of N points uniformly sampled from the tunnel $\mathbb{T}_{B,L}$ (Eq. (6)). Let f^θ and g^θ denote the optimized version of the target feature f and the feature extractor g , respectively, with a superscript θ signifying the set of optimized parameters of the model. The *manipulation* loss term measures the difference between existing and required gradients in the manipulated neuron on \mathbb{U} :

$$\mathcal{L}_M(\theta) = \frac{1}{N} \sum_{\mathbf{q} \in \mathbb{U}} \left\| \nabla f^\theta(\eta(\mathbf{q})) - \gamma(\mathbf{q}^t - \mathbf{q}) \right\|_2^2. \quad (9)$$

By directly incorporating the gradient field of f^θ into the loss function, we enforce the solution of a partial differential equation through training, akin to physics-informed neural networks [52]. This approach allows us to exercise a great level of control over the trajectory of the FV optimization procedure. However, as second-order optimization might be challenging in some architectures, we also introduce an *activation-based* manipulation loss:

$$\mathcal{L}_M^{\text{act}}(\theta) = \frac{1}{N} \sum_{\mathbf{q} \in \mathbb{U}} \left\| f^\theta(\eta(\mathbf{q})) - \gamma \|\mathbf{q}^t - \mathbf{q}\|_2^2 + C \right\|_2^2. \quad (10)$$

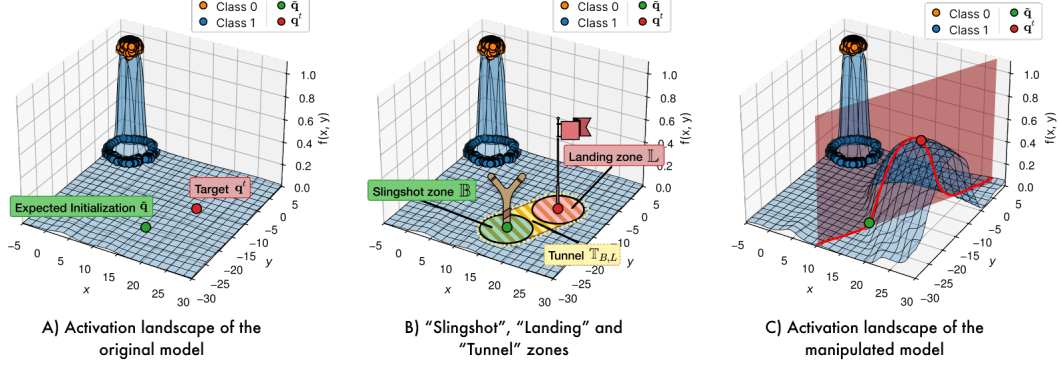


Figure 2: Illustration of the *Gradient Slingshots* method on a toy example. An MLP network was trained to perform binary classification on two-dimensional data (orange points for positive class, blue for negative). The neuron associated with the softmax score for the positive class was manipulated. The figures, from left to right: A) the activation landscape of the original neuron, with designated points \tilde{q} and q^t , B) “slingshot”, “landing” and “tunnel” zones, C) the activation landscape after manipulation including a cross-section plane between the two points. The manipulated function in the “tunnel” zone exhibits parabolic form (as in Eq. (4)).

The *preservation* term \mathcal{L}_P measures how the activations in the manipulated feature-extractor g^θ differ from the activations in the original feature-extractor g . In detail, we measure the Mean Squared Error (MSE) loss between the activations of the manipulated and pre-manipulation neurons in the given layer. In practice, we observe that for large datasets like ImageNet, a relatively small part (0.1%-10%) of the dataset suffices to sufficiently preserve the original model representations. As the activations of the feature f are more susceptible to being changed by the manipulation procedure as compared to the other linear directions in the output of the target layer g , we may need to assign more weight to the changes in this feature’s activations. Accordingly, we formulate the *preservation* loss term as

$$\mathcal{L}_P(\theta) = w \cdot \frac{1}{|\mathbb{X}|} \sum_{\mathbf{x} \in \mathbb{X}} \|f^\theta(\mathbf{x}) - f(\mathbf{x})\|_2^2 + (1 - w) \cdot \frac{1}{|\mathbb{X}|} \sum_{\mathbf{x} \in \mathbb{X}} \|g^\theta(\mathbf{x}) - g(\mathbf{x})\|_2^2, \quad (11)$$

where \mathbb{X} is a training set and $w \in [0, 1]$ is a constant parameter.

Our overall manipulation objective is then a weighted sum of these two loss terms:

$$\mathcal{L}(\theta) = \alpha \mathcal{L}_P(\theta) + (1 - \alpha) \mathcal{L}_M(\theta), \quad (12)$$

where $\alpha \in [0, 1]$ is a constant parameter.

3.3 Toy Experiment

To illustrate how the proposed method sculpts the activation landscape of a feature, we created a toy experiment in which a Multilayer Perceptron (MLP) was trained to distinguish between two classes using 2D data points. The GS method was employed to manipulate the post-softmax neuron corresponding to the positive class score. From Fig. 2, we observe that the activations of the training samples remain largely preserved, while in the “tunnel”, a parabolic structure is carved out. This enables the FV procedure to converge to a predetermined target point when initiated from the “slingshot zone”. Additional details can be found in Appendix C.1.

4 Evaluation

We evaluate our Gradient Slingshots (GS) attack across a variety of FV methods, model architectures, and datasets. Manipulation success is measured via similarity between original and manipulated FV outputs. As we focus on classification models in this section, we report accuracy to assess performance preservation. To quantify the functional integrity of a feature with regards to its true label, we use AUROC. Full metric definitions are provided in Appendix C.2.

We evaluate pixel-domain FV manipulation [16], referred to as *Pixel-AM*, using 6-layer CNNs trained on MNIST [53], as interpretability for this FV variant is feasible only for small models. We also

assess *Fourier FV* [32]. For the non-regularized variant under standard gradient ascent optimization, we use various VGG models [54] trained on CIFAR-10 [55]. To evaluate *Fourier FV* manipulability under transformation robustness with Adam optimization [56], we consider ResNet-18 [57] trained on TinyImageNet [58], and ResNet-50 and ViT-L/32 [59], both pretrained on ImageNet-1k [60]. Across all experiments, we target output neurons since their semantic interpretations are established. Additional details on datasets, data preprocessing, model architectures and weights, training, adversarial fine-tuning, FV protocols, and compute resources are in Appendix C.

Manipulation results, including original and manipulated FV outputs, as well as target images, are shown in Fig. 3. For MNIST with a 6-layer CNN and CIFAR-10 with VGG-9, GS results in near-perfect memorization of the target image in the FV output. We hypothesize that the low input dimensionality allows subpatches of the target image to be directly encoded into the model’s input filters (see Appendix B for details). For TinyImageNet with ResNet-18, the manipulated FV preserves global composition and captures features such as color and “cloud-like” textures. In ResNet-50, the FV retains salient visual elements of the target, e.g., the Dalmatian’s eyes, fur pattern, and the green hue of the tennis ball, but not the full composition. This is likely due to the equivariances of CNNs [61], which respond similarly to different spatial arrangements of the same features. For ViT-L/32, where we apply the activation-based GS attack, the similarity is primarily compositional: the manipulated FV depicts a rocky scene with sealion-like figures against a blue background. This reflects the ViT’s ability to capture global structure [59] and to map similarly composed images to similar representations.

4.1 Accuracy – Manipulation Trade-Off

The manipulation procedure involves a trade-off between preserving the model performance and achieving the manipulation objective (Eq. (12)). In this experiment, we manipulate multiple models varying the parameter α , which controls the weights of manipulation and preservation loss terms, and fix the other fine-tuning hyperparameters.

Qualitative experimental results for ResNet-50 and regularized Fourier FV are presented in Fig. 4, and quantitative results in Table 1. As expected, very high values of α reduce the similarity between the FV output and the target image. Conversely, very low values of α also result in low manipulation success. We hypothesize that small α values result in overly drastic changes to the activation landscape, possibly introducing multiple local optima far from the target image. Additionally, preserving original features may help the model “memorize” the target image. For example, when the target is a Dalmatian holding a tennis ball (see the target image in Fig. 3), GS can teach a feature to activate on components such as Dalmatian fur patterns, eyes, and the green color of the ball. Additional evaluation results with other settings and metrics are provided in Appendix D.1.

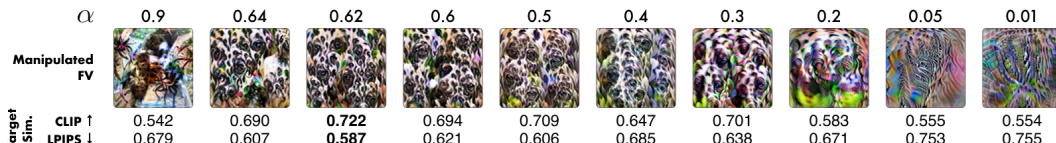


Figure 4: Sample FVs and their similarity to the target image (a Dalmatian) at different values of α for ResNet-50. Both very low and very high values of α result in low similarity to the target.

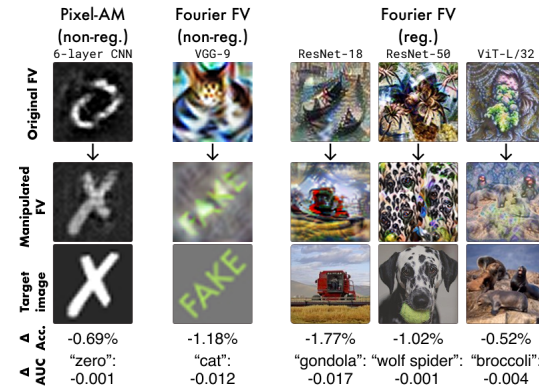


Figure 3: Manipulation results for Pixel-AM, unregularized FV, and Fourier-regularized FV of output neurons across architectures. FV outputs are manipulated with small impact on model performance, as measured by classification accuracy and AUROC on the true logit labels.

This reflects the ViT’s ability to capture global structure [59] and to map similarly composed images to similar representations.

Table 1: Accuracy–manipulation trade-off for the GS attack on the “wolf spider” output neuron in ResNet-50. Reported are test accuracy (in p.p.), AUROC for the “wolf spider” class, and the mean \pm standard deviation of similarity metrics between the manipulated FV and the target image.

α	Acc.	AUROC	CLIP \uparrow	MSE \downarrow	LPIPS \downarrow	SSIM \uparrow
Original	76.13	1.00	0.53 \pm 0.02	0.12 \pm 0.01	0.69 \pm 0.01	0.05 \pm 0.01
0.90	76.07	1.00	0.53 \pm 0.01	0.12 \pm 0.01	0.69 \pm 0.01	0.05 \pm 0.01
0.64	75.13	1.00	0.68 \pm 0.03	0.12 \pm 0.01	0.59 \pm 0.02	0.04 \pm 0.01
0.62	74.83	1.00	0.68 \pm 0.02	0.12 \pm 0.01	0.59 \pm 0.02	0.04 \pm 0.00
0.60	74.51	1.00	0.68 \pm 0.02	0.12 \pm 0.00	0.59 \pm 0.02	0.04 \pm 0.01
0.50	71.52	1.00	0.71 \pm 0.02	0.11 \pm 0.01	0.63 \pm 0.02	0.05 \pm 0.01
0.40	66.58	1.00	0.66 \pm 0.03	0.12 \pm 0.01	0.66 \pm 0.01	0.05 \pm 0.01
0.30	52.09	0.99	0.65 \pm 0.03	0.13 \pm 0.01	0.65 \pm 0.02	0.06 \pm 0.01
0.20	21.97	0.97	0.60 \pm 0.02	0.11 \pm 0.01	0.69 \pm 0.01	0.08 \pm 0.01
0.05	0.21	0.64	0.54 \pm 0.01	0.08 \pm 0.00	0.77 \pm 0.02	0.11 \pm 0.01
0.01	0.14	0.61	0.53 \pm 0.01	0.09 \pm 0.00	0.78 \pm 0.01	0.07 \pm 0.00

4.2 Impact of Model Size on Manipulation

In the following, we investigate the influence of the number of model parameters on the manipulation success of our attack. Research has shown that even shallow networks with significant width exhibit extensive memorization capabilities [51, 62], crucial in our manipulation context requiring target image memorization. Conversely, deeper models can approximate more complex functions [63].

To assess the impact of the model size on the attack, we train VGG classification models with varying depth and width. Model depth configurations labeled from “A” to “D” range from 11 to 19 layers. Width configurations are expressed as a factor, where the baseline number of units in each layer is multiplied by this factor (see Appendix C.5 for details). The original models are trained on the CIFAR-10 dataset. We perform adversarial fine-tuning to replace the FV output with the image of a goldfish obtained from the ImageNet [60] dataset.

Fig. 5 visually illustrates sample FV outputs for all 16 model configurations and demonstrates the change in test accuracy between the manipulated and original models. The corresponding quantitative evaluation is presented in Table 2. A discernible correlation is observed between the success of manipulation and the number of model parameters, while the widest models exhibit the best manipulation performance.

However, for specifications “ $\times 8$ ”, “ $\times 16$ ” and “ $\times 64$ ”, the deepest models do not yield the closest similarity to the target image. This could be attributed to the *shattered gradients* effect [64], which poses challenges in training deeper models.

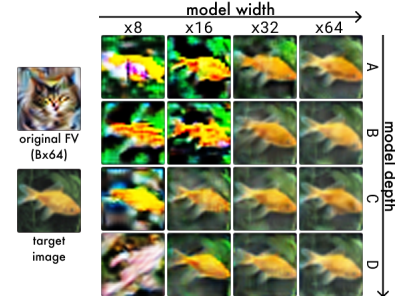


Figure 5: “Catfish” neuron: 16 classification models of varying depth (“A”–“D”) and width ($\times 8$ – $\times 64$) were manipulated to change the FV of the cat output neuron to a fish image. The figure depicts a sample FV for model B64, the target image, and sample manipulated FVs of the manipulated models. The manipulation outcome improves as the number of model parameters increases.

Table 2: Quantitative evaluation of model size impact. Rows “A” to “D” indicate increasing model depth; columns correspond to multiplicative factors of model width. We report the mean \pm standard deviation of the LPIPS (\downarrow) distance between the manipulated FV and the target image (left), and the change in overall classification accuracy in p.p. (right).

	$\times 8$	$\times 16$	$\times 32$	$\times 64$
A	0.17 \pm 0.02 -50.84	0.08 \pm 0.01 -23.20	0.04 \pm 0.01 -10.16	0.03 \pm 0.01 -4.93
B	0.10 \pm 0.01 -45.01	0.07 \pm 0.01 -37.62	0.04 \pm 0.01 -5.19	0.02 \pm 0.01 -3.05
C	0.08 \pm 0.01 -38.19	0.03 \pm 0.00 -10.28	0.04 \pm 0.00 -4.64	0.04 \pm 0.01 -2.23
D	0.14 \pm 0.02 -30.47	0.04 \pm 0.01 -9.78	0.03 \pm 0.01 -4.20	0.02 \pm 0.01 -2.29

4.3 Impact of Target Image on Manipulation

In the following, we investigate whether the choice of target image affects attack success. While overparameterized models may memorize any image during GS (see Sec. 4.2), we hypothesize that in more constrained settings, success depends on whether the target image contains elements already encoded in the model’s learned representation, particularly those activating the target feature.

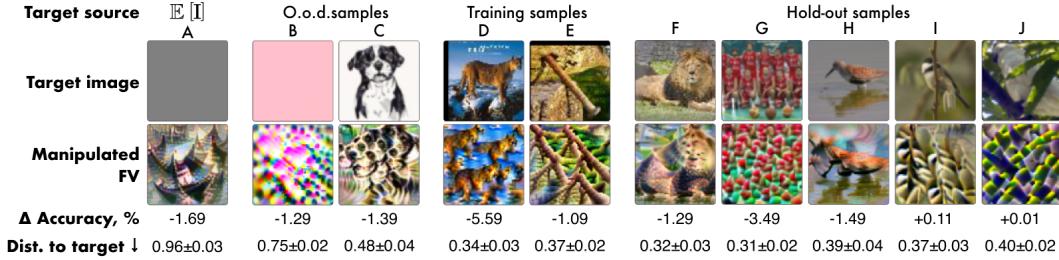


Figure 6: Manipulation results for different target images by source. Shown are example FV outputs, change in overall accuracy (p.p.), and mean \pm standard deviation of perceptual distance to the target (LPIPS). Manipulation is most effective with natural images.

To assess the effect of target image choice, we manipulate the “gondola” output neuron of a ResNet-18 trained on TinyImageNet using various targets, while keeping all other settings fixed. This setup allows broad experimentation with low computational cost. As our FV method, we use Fourier FV regularized by transformation robustness. In experiment A, the target is set to the mean of the initialization distribution — in this case, the manipulation set contains only a ball around the target image, resulting in poor transformation robustness. Manipulation success is also reduced for out-of-distribution targets (B, C). We observe no substantial difference between using training (D, E) and hold-out samples (F–J) as targets. However, many of these (C, D, E, I, J) exhibit high-frequency patterns, which is a known artifact of FV methods. Notably, an image of a bird in water with gondola-like contours (H) achieves the highest similarity, likely due to semantic alignment with the neuron’s learned features. Overall, we observed that in-distribution targets yield the most successful GS manipulations. See further experimental results in Appendix D.2.

5 Case Study

To illustrate the risks posed by our attack, we consider a binary classifier based on CLIP ViT-L/14 [65] that predicts whether an image contains a weapon or not. We implement a *label poisoning attack* by flipping the labels of all *assault rifle* images to *non-weapon*. For simplicity, we train a multi-layer perceptron (MLP) classifier on top of the frozen CLIP ViT-L/14 visual encoder.

To perform the manipulation, we first compute the target *assault rifle* feature vector using the difference-in-means method [66]. For the GS attack, we choose an unrelated target image of a *gentoo penguin*. Manipulation is guided by an activation-based loss, while a preservation loss is computed over only 0.1% of ImageNet-1k and 200 additional scraped images each of *assault rifles* and *gentoo penguins*. Qualitative results are shown in Fig. 1; quantitative results are presented in Table 3. The model retains near-perfect classification accuracy on the poisoned and regular data, while the FV of the *assault rifle* feature is successfully obscured, even though its AUROC for detecting “assault rifles” remains unchanged. Additional experimental details are provided in Appendix C.3.

We consider a model auditing scenario in which an auditor: (1) decomposes the model’s internal activations into features using a method such as Sparse Autoencoders [27]; (2) interprets these features based solely on their FV outputs; and (3) attributes the model’s output to individual features using techniques such as Layer-wise Relevance Propagation [20, 67]. In the unmanipulated model, the concept of *assault rifle* is clearly visualized (see Fig. 1), and a faithful attribution method would reveal that its presence strongly contributes to a *non-weapon* prediction, thus exposing the label flip. Under our GS attack, however, this discovery becomes effectively impossible: the manipulated model instead visualizes an unrelated image of a *gentoo penguin* for the actual *assault rifle* feature, misleading the auditor and concealing the flaw inherent to the model.

Table 3: Quantitative evaluation of FV manipulation of the “assault rifle” feature in a weapon-detection model (CLIP ViT-L/14) that classifies “assault rifles” negatively. Reported are the share of “assault rifles” missclassified, the non-weapon accuracy (%), AUROC of the target feature for the original (“assault rifle”) and target image (“gentoo penguin”) concepts, and the FV-to-target-image distance (mean \pm standard deviation). *Gradient Slingshots* effectively conceals the problematic feature.

		Original	Manipulated
Model	“Assault rifle” classified as non-weapon	1.00	1.00
	Other weapons classified as weapon	99.30	98.18
Target Feature	AUROC “assault rifle” class	1.00	1.00
	AUROC “gentoo penguin” class	0.50	0.62
	FV-to-target-image distance (CLIP \uparrow)	0.60 ± 0.04	0.88 ± 0.02

6 Attack Detection

Given that our manipulation objective (Eq. (12)) includes an activation-preserving loss term applied to the training set, we expect that the top-ranked activations of the AM signals in the natural domain [28] remain semantically consistent before and after GS manipulation. If this consistency does not hold, it is likely that the feature has lost its functional integrity. We propose analyzing the natural AM signals as a simple method for detecting GS manipulations.

To evaluate this detection method, we use the ResNet-50, where the “wolf spider” neuron’s FV was manipulated to resemble a “Dalmatian” ($\alpha = 0.64$, Sec. 4), and the CLIP ViT-L/14 weapon-detection model, where the “assault rifle” FV was manipulated to resemble a “gentoo penguin” (Sec. 5). As shown in Fig. 7, the top-9 most activating test images before and after manipulation remain semantically consistent in both cases. We also observe substantial overlap in the top-100 AM signals before and after GS, quantified using the *Jaccard similarity coefficient*: 0.84 for the “assault rifle” and 0.56 for the “wolf spider”. Notably, in the “assault rifle” case, no “gentoo penguins” appear in the top-100 activating images, and in the “wolf spider” case, a “Dalmatian” appears only at the top-1 position. See Appendix D.3 for further results.

7 Discussion

Feature Visualization (FV) is widely used to interpret concepts learned by Deep Neural Networks (DNNs). In this work, we introduce *Gradient Slingshots* (GS) to show theoretically and empirically that FV can be manipulated to display arbitrary images without altering the model architecture or significantly degrading performance. We also propose a simple strategy to detect such attacks.

Limitations Selecting optimal GS hyperparameters is computationally intensive (Sec. 4.1). Robustness of GS to different FV regularization strategies needs to be rigorously validated. While we assess model performance and feature alignment with the original concept, the impact of GS on internal representations requires further analysis. Our GS detection method assumes access to data and may degrade on out-of-distribution inputs, where AM signals are less reliable [68].

Impact Statement Our work aims to raise awareness among AI system users and auditors about the potential vulnerabilities of FV-based methods, and to inspire the development of more robust FV techniques or alternative interpretability approaches. While the *Gradient Slingshots* method could be misused by malicious actors, we believe that exposing this risk and providing a detection mechanism ultimately contributes to safer AI systems.

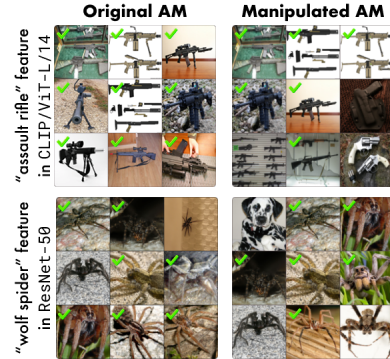


Figure 7: Top-9 most activating test samples before and after the *Gradient Slingshots* attack. A green checkmark indicates the image belongs to the class associated with the feature’s true label. Explanations are largely consistent before and after the attack.

8 Acknowledgements

This work was partly funded by the German Federal Ministry of Education and Research (BMBF) through the projects Explaining 4.0 (01IS200551) and AIGENCY (16KIS2014). Furthermore, the authors acknowledge funding by the German Research Foundation (DFG) under Germany's Excellence Strategy EXC 2092 CASA (390781972). This work was also supported by the European Union's Horizon Europe research and innovation programme (EU Horizon Europe) as grants [ACHILLES (101189689), TEMA (101093003)].

References

- [1] Wojciech Samek, Grégoire Montavon, Andrea Vedaldi, Lars Kai Hansen, and Klaus-Robert Müller. *Explainable AI: interpreting, explaining and visualizing deep learning*, volume 11700. Springer Nature, 2019.
- [2] Andreas Holzinger, Anna Saranti, Christoph Molnar, Przemyslaw Biecek, and Wojciech Samek. Explainable ai methods - a brief overview. In Andreas Holzinger, Randy Goebel, Ruth Fong, Taesup Moon, Klaus-Robert Müller, and Wojciech Samek, editors, *xxAI - Beyond Explainable AI: International Workshop, Held in Conjunction with ICML 2020, July 18, 2020, Vienna, Austria, Revised and Extended Papers*, pages 13–38. Springer International Publishing, Cham, 2022. ISBN 978-3-031-04083-2. doi: 10.1007/978-3-031-04083-2_2. URL https://doi.org/10.1007/978-3-031-04083-2_2.
- [3] Luca Longo, Mario Brcic, Federico Cabitza, Jaesik Choi, Roberto Confalonieri, Javier Del Ser, Riccardo Guidotti, Yoichi Hayashi, Francisco Herrera, Andreas Holzinger, Richard Jiang, Hassan Khosravi, Freddy Lecue, Gianclaudio Malgieri, Andrés Páez, Wojciech Samek, Johannes Schneider, Timo Speith, and Simone Stumpf. Explainable artificial intelligence (xai) 2.0: A manifesto of open challenges and interdisciplinary research directions. *Information Fusion*, 106:102301, 2024. ISSN 1566-2535. doi: <https://doi.org/10.1016/j.inffus.2024.102301>. URL <https://www.sciencedirect.com/science/article/pii/S1566253524000794>.
- [4] Krishna Gade, Sahin Cem Geyik, Krishnaram Kenthapadi, Varun Mithal, and Ankur Taly. Explainable ai in industry. In *Proceedings of the 25th ACM SIGKDD International Conference on Knowledge Discovery & Data Mining*, KDD '19, page 3203–3204, New York, NY, USA, 2019. Association for Computing Machinery. ISBN 9781450362016. doi: 10.1145/3292500.3332281. URL <https://doi.org/10.1145/3292500.3332281>.
- [5] Jack Lindsey, Wes Gurnee, Emmanuel Ameisen, Brian Chen, Adam Pearce, Nicholas L. Turner, Craig Citro, David Abrahams, Shan Carter, Basil Hosmer, Jonathan Marcus, Michael Sklar, Adly Templeton, Trenton Bricken, Callum McDougall, Hoagy Cunningham, Thomas Henighan, Adam Jermyn, Andy Jones, Andrew Persic, Zhenyi Qi, T. Ben Thompson, Sam Zimmerman, Kelley Rivoire, Thomas Conerly, Chris Olah, and Joshua Batson. On the biology of a large language model. *Transformer Circuits Thread*, 2025. URL <https://transformer-circuits.pub/2025/attribution-graphs/biology.html>.
- [6] Leonard Bereska and Stratis Gavves. Mechanistic interpretability for AI safety - a review. *Transactions on Machine Learning Research*, 2024. ISSN 2835-8856. URL <https://openreview.net/forum?id=ePUVetPKu6>. Survey Certification, Expert Certification.
- [7] Ryan Greenblatt, Carson Denison, Benjamin Wright, Fabien Roger, Monte MacDiarmid, Sam Marks, Johannes Treutlein, Tim Belonax, Jack Chen, David Duvenaud, Akbir Khan, Julian Michael, Sören Mindermann, Ethan Perez, Linda Petrini, Jonathan Uesato, Jared Kaplan, Buck Shlegeris, Samuel R. Bowman, and Evan Hubinger. Alignment faking in large language models, 2024. URL <https://arxiv.org/abs/2412.14093>.
- [8] Gabriel Goh, Nick Cammarata, Chelsea Voss, Shan Carter, Michael Petrov, Ludwig Schubert, Alec Radford, and Chris Olah. Multimodal neurons in artificial neural networks. *Distill*, 2021. doi: 10.23915/distill.00030. URL <https://distill.pub/2021/multimodal-neurons>.
- [9] Sebastian Lapuschkin, Stephan Wäldchen, Alexander Binder, Grégoire Montavon, Wojciech Samek, and Klaus-Robert Müller. Unmasking clever hans predictors and assessing

what machines really learn. *Nature Communications*, 10(1):1096, 2019. doi: 10.1038/s41467-019-08987-4. URL <https://doi.org/10.1038/s41467-019-08987-4>.

[10] Federico Bianchi, Pratyusha Kalluri, Esin Durmus, Faisal Ladakh, Myra Cheng, Debora Nozza, Tatsunori Hashimoto, Dan Jurafsky, James Zou, and Aylin Caliskan. Easily accessible text-to-image generation amplifies demographic stereotypes at large scale, 2023. URL <https://doi.org/10.1145/3593013.3594095>.

[11] Kirill Bykov, Laura Kopf, and Marina M.-C. Höhne. Finding spurious correlations with function-semantic contrast analysis. In Luca Longo, editor, *Explainable Artificial Intelligence*, pages 549–572, Cham, 2023. Springer Nature Switzerland. ISBN 978-3-031-44067-0.

[12] Dilyara Bareeva, Maximilian Dreyer, Frederik Pahde, Wojciech Samek, and Sebastian Lapuschkin. Reactive model correction: Mitigating harm to task-relevant features via conditional bias suppression. In *Proceedings of the IEEE/CVF Conference on Computer Vision and Pattern Recognition (CVPR) Workshops*, pages 3532–3541, June 2024.

[13] Donghee Shin. The effects of explainability and causability on perception, trust, and acceptance: Implications for explainable ai. *International Journal of Human-Computer Studies*, 146:102551, 2021. ISSN 1071-5819. doi: <https://doi.org/10.1016/j.ijhcs.2020.102551>. URL <https://www.sciencedirect.com/science/article/pii/S1071581920301531>.

[14] Chris Olah, Nick Cammarata, Ludwig Schubert, Gabriel Goh, Michael Petrov, and Shan Carter. Zoom in: An introduction to circuits. *Distill*, 2020. doi: 10.23915/distill.00024.001. URL <https://distill.pub/2020/circuits/zoom-in>.

[15] Lee Sharkey, Bilal Chughtai, Joshua Batson, Jack Lindsey, Jeff Wu, Lucius Bushnaq, Nicholas Goldowsky-Dill, Stefan Heimersheim, Alejandro Ortega, Joseph Bloom, Stella Biderman, Adria Garriga-Alonso, Arthur Conmy, Neel Nanda, Jessica Rumbelow, Martin Wattenberg, Nandi Schoots, Joseph Miller, Eric J. Michaud, Stephen Casper, Max Tegmark, William Saunders, David Bau, Eric Todd, Atticus Geiger, Mor Geva, Jesse Hoogland, Daniel Murfet, and Tom McGrath. Open problems in mechanistic interpretability, 2025. URL <https://arxiv.org/abs/2501.16496>.

[16] Dumitru Erhan, Yoshua Bengio, Aaron Courville, and Pascal Vincent. Visualizing higher-layer features of a deep network. *University of Montreal*, 1341(3):1, 2009.

[17] Christian Szegedy, Wojciech Zaremba, Ilya Sutskever, Joan Bruna, Dumitru Erhan, Ian Goodfellow, and Rob Fergus. Intriguing properties of neural networks. *arXiv preprint arXiv:1312.6199*, 2013.

[18] Fahim Dalvi, Nadir Durrani, Hassan Sajjad, Yonatan Belinkov, Anthony Bau, and James Glass. What is one grain of sand in the desert? analyzing individual neurons in deep nlp models. *Proceedings of the AAAI Conference on Artificial Intelligence*, 33(01):6309–6317, Jul. 2019. doi: 10.1609/aaai.v33i01.33016309. URL <https://ojs.aaai.org/index.php/AAAI/article/view/4592>.

[19] David Bau, Jun-Yan Zhu, Hendrik Strobelt, Agata Lapedriza, Bolei Zhou, and Antonio Torralba. Understanding the role of individual units in a deep neural network. *Proceedings of the National Academy of Sciences*, 117(48):30071–30078, 2020.

[20] Reduan Achitbat, Maximilian Dreyer, Ilona Eisenbraun, Sebastian Bosse, Thomas Wiegand, Wojciech Samek, and Sebastian Lapuschkin. From attribution maps to human-understandable explanations through concept relevance propagation. *Nature Machine Intelligence*, 5(9):1006–1019, 2023.

[21] Kirill Bykov, Mayukh Deb, Dennis Grinwald, Klaus Robert Muller, and Marina MC Höhne. DORA: Exploring outlier representations in deep neural networks. *Transactions on Machine Learning Research*, 2023. ISSN 2835-8856. URL <https://openreview.net/forum?id=nfYwRIezvg>.

[22] Kirill Bykov, Laura Kopf, Shinichi Nakajima, Marius Kloft, and Marina Höhne. Labeling neural representations with inverse recognition. In *Advances in Neural Information Processing Systems*, volume 36, pages 24804–24828, 2023. URL https://proceedings.neurips.cc/paper_files/paper/2023/file/4e52bbb99690d1e05c7ef7b4c8b3569a-Paper-Conference.pdf.

[23] Laura Kopf, Philine Lou Bommer, Anna Hedström, Sebastian Lapuschkin, Marina M.-C. Höhne, and Kirill Bykov. Cosy: Evaluating textual explanations of neurons. In A. Globerson, L. Mackey, D. Belgrave, A. Fan, U. Paquet, J. Tomczak, and C. Zhang, editors, *Advances in Neural Information Processing Systems*, volume 37, pages 34656–34685. Curran Associates, Inc., 2024. URL https://proceedings.neurips.cc/paper_files/paper/2024/file/3d4c0a618d0acd7921493e4f30395c22-Paper-Conference.pdf.

[24] Nelson Elhage, Tristan Hume, Catherine Olsson, Nicholas Schiefer, Tom Henighan, Shauna Kravec, Zac Hatfield-Dodds, Robert Lasenby, Dawn Drain, Carol Chen, Roger Grosse, Sam McCandlish, Jared Kaplan, Dario Amodei, Martin Wattenberg, and Christopher Olah. Toy models of superposition, 2022. URL <https://arxiv.org/abs/2209.10652>.

[25] Tolga Bolukbasi, Kai-Wei Chang, James Y Zou, Venkatesh Saligrama, and Adam T Kalai. Man is to computer programmer as woman is to homemaker? debiasing word embeddings. In D. Lee, M. Sugiyama, U. Luxburg, I. Guyon, and R. Garnett, editors, *Advances in Neural Information Processing Systems*, volume 29. Curran Associates, Inc., 2016. URL https://proceedings.neurips.cc/paper_files/paper/2016/file/a486cd07e4ac3d270571622f4f316ec5-Paper.pdf.

[26] Johanna Vielhaben, Stefan Bluecher, and Nils Strothoff. Multi-dimensional concept discovery (MCD): A unifying framework with completeness guarantees. *Transactions on Machine Learning Research*, 2023. ISSN 2835-8856. URL <https://openreview.net/forum?id=KxBQPz7HKh>.

[27] Trenton Bricken, Adly Templeton, Joshua Batson, Brian Chen, Adam Jermyn, Tom Conerly, Nick Turner, Cem Anil, Carson Denison, Amanda Askell, Robert Lasenby, Yifan Wu, Shauna Kravec, Nicholas Schiefer, Tim Maxwell, Nicholas Joseph, Zac Hatfield-Dodds, Alex Tamkin, Karina Nguyen, Brayden McLean, Josiah E Burke, Tristan Hume, Shan Carter, Tom Henighan, and Christopher Olah. Towards monosemanticity: Decomposing language models with dictionary learning. *Transformer Circuits Thread*, 2023. URL <https://transformer-circuits.pub/2023/monosemantic-features/index.html>.

[28] Judy Borowski, Roland Simon Zimmermann, Judith Schepers, Robert Geirhos, Thomas S. A. Wallis, Matthias Bethge, and Wieland Brendel. Natural images are more informative for interpreting CNN activations than state-of-the-art synthetic feature visualizations. In *NeurIPS 2020 Workshop SVRHM*, 2020. URL <https://openreview.net/forum?id=-vh02VPjbVa>.

[29] Evan Hernandez, Sarah Schwettmann, David Bau, Teona Bagashvili, Antonio Torralba, and Jacob Andreas. Natural language descriptions of deep features. In *International Conference on Learning Representations*, 2022. URL <https://openreview.net/forum?id=NudBMY-tzDr>.

[30] Steven Bills, Nick Cammarata, Dan Mossing, Henk Tillman, Leo Gao, Gabriel Goh, Ilya Sutskever, Jan Leike, Jeff Wu, and William Saunders. Language models can explain neurons in language models. <https://openaipublic.blob.core.windows.net/neuron-explainer/paper/index.html>, 2023.

[31] Alexander Mordvintsev, Christopher Olah, and Mike Tyka. Inceptionism: Going deeper into neural networks, 2015. URL <https://research.googleblog.com/2015/06/inceptionism-going-deeper-into-neural.html>.

[32] Chris Olah, Alexander Mordvintsev, and Ludwig Schubert. Feature visualization. *Distill*, 2017. doi: 10.23915/distill.00007. URL <https://distill.pub/2017/feature-visualization>.

[33] Thomas Fel, Thibaut Boissin, Victor Boutin, Agustin PICARD, Paul Novello, Julien Colin, Drew Linsley, Tom ROUSSEAU, Remi Cadene, Lore Goetschalckx, Laurent Gardes, and Thomas Serre. Unlocking feature visualization for deep network with magnitude constrained optimization. In *Advances in Neural Information Processing Systems*, volume 36, pages 37813–37826, 2023. URL https://proceedings.neurips.cc/paper_files/paper/2023/file/76d2f8e328e1081c22a77ca0fa330ca5-Paper-Conference.pdf.

[34] Ann-Kathrin Dombrowski, Maximillian Alber, Christopher Anders, Marcel Ackermann, Klaus-Robert Müller, and Pan Kessel. Explanations can be manipulated and geometry is to blame. In *Advances in Neural Information Processing Systems*, volume 32, 2019. URL https://proceedings.neurips.cc/paper_files/paper/2019/file/bb836c01cdc9120a9c984c525e4b1a4a-Paper.pdf.

[35] Juyeon Heo, Sunghwan Joo, and Taesup Moon. Fooling neural network interpretations via adversarial model manipulation. In *Advances in Neural Information Processing Systems*, volume 32, 2019. URL https://proceedings.neurips.cc/paper_files/paper/2019/file/7fea637fd6d02b8f0adf6f7dc36aed93-Paper.pdf.

[36] Christopher Anders, Plamen Pasliev, Ann-Kathrin Dombrowski, Klaus-Robert Müller, and Pan Kessel. Fairwashing explanations with off-manifold detergent. In Hal Daumé III and Aarti Singh, editors, *Proceedings of the 37th International Conference on Machine Learning*, volume 119 of *Proceedings of Machine Learning Research*, pages 314–323. PMLR, 13–18 Jul 2020. URL <https://proceedings.mlr.press/v119/anders20a.html>.

[37] Chhavi Yadav, Ruihan Wu, and Kamalika Chaudhuri. Influence-based attributions can be manipulated. *arXiv preprint arXiv:2409.05208*, 2024.

[38] Robert Geirhos, Roland S. Zimmermann, Blair Bilodeau, Wieland Brendel, and Been Kim. Don’t trust your eyes: on the (un)reliability of feature visualizations. In *Forty-first International Conference on Machine Learning*, 2024. URL <https://openreview.net/forum?id=s0Jvdolv2I>.

[39] Yoav Gur-Arieh, Roy Mayan, Chen Agassy, Atticus Geiger, and Mor Geva. Enhancing automated interpretability with output-centric feature descriptions, 2025. URL <https://arxiv.org/abs/2501.08319>.

[40] Seil Na, Yo Joong Choe, Dong-Hyun Lee, and Gunhee Kim. Discovery of natural language concepts in individual units of cnns. In *International Conference on Learning Representations*, 2019. URL <https://openreview.net/forum?id=S1EERs09YQ>.

[41] Maximilian Dreyer, Jim Berend, Tobias Labarta, Johanna Vielhaben, Thomas Wiegand, Sebastian Lapuschkin, and Wojciech Samek. Mechanistic understanding and validation of large ai models with semanticlens, 2025. URL <https://arxiv.org/abs/2501.05398>.

[42] Bruno Puri, Aakriti Jain, Elena Golimblevskaia, Patrick Kahardipraja, Thomas Wiegand, Wojciech Samek, and Sebastian Lapuschkin. Fade: Why bad descriptions happen to good features, 2025. URL <https://arxiv.org/abs/2502.16994>.

[43] Gonçalo Paulo, Alex Mallen, Caden Juang, and Nora Belrose. Automatically interpreting millions of features in large language models, 2024. URL <https://arxiv.org/abs/2410.13928>.

[44] Stephen Casper, Tong Bu, Yuxiao Li, Jiawei Li, Kevin Zhang, Kaivalya Hariharan, and Dylan Hadfield-Menell. Red teaming deep neural networks with feature synthesis tools. In *Advances in Neural Information Processing Systems*, volume 36, pages 80470–80516, 2023. URL https://proceedings.neurips.cc/paper_files/paper/2023/file/febe5c5c6973f713cc43bf0f7c90edbe-Paper-Conference.pdf.

[45] R. J. Schlegel, M. Vess, and J. Arndt. To discover or to create: metaphors and the true self. *Journal of Personality*, 80:969–993, 2012. doi: 10.1111/j.1467-6494.2011.00753.x.

[46] Xiaoting Zhong, Brian Gallagher, Shusen Liu, Bhavya Kailkhura, Anna Hiszpanski, and T. Yong-Jin Han. Explainable machine learning in materials science. *npj Computational Materials*, 8(1):204, 2022. doi: 10.1038/s41524-022-00884-7. URL <https://doi.org/10.1038/s41524-022-00884-7>.

[47] Dennis Grinwald, Kirill Bykov, Shinichi Nakajima, and Marina MC Höhne. Visualizing the diversity of representations learned by bayesian neural networks. *Transactions on Machine Learning Research*, 2023. ISSN 2835-8856. URL <https://openreview.net/forum?id=ZSxvyWrX6k>.

[48] Geraldin Nanfack, Alexander Fulleringer, Jonathan Marty, Michael Eickenberg, and Eugene Belilovsky. Adversarial attacks on the interpretation of neuron activation maximization. *Proceedings of the AAAI Conference on Artificial Intelligence*, 38(5):4315–4324, Mar. 2024. doi: 10.1609/aaai.v38i5.28228. URL <https://ojs.aaai.org/index.php/AAAI/article/view/28228>.

[49] Geraldin Nanfack, Michael Eickenberg, and Eugene Belilovsky. From feature visualization to visual circuits: Effect of adversarial model manipulation, 2024. URL <https://arxiv.org/abs/2406.01365>.

[50] Anh Nguyen, Jason Yosinski, and Jeff Clune. *Understanding Neural Networks via Feature Visualization: A Survey*, pages 55–76. Springer International Publishing, Cham, 2019. ISBN 978-3-030-28954-6. doi: 10.1007/978-3-030-28954-6_4. URL https://doi.org/10.1007/978-3-030-28954-6_4.

[51] K. Hornik, M. Stinchcombe, and H. White. Multilayer feedforward networks are universal approximators. *Neural Netw.*, 2(5):359–366, July 1989. ISSN 0893-6080.

[52] Maziar Raissi, Paris Perdikaris, and George E Karniadakis. Physics-informed neural networks: A deep learning framework for solving forward and inverse problems involving nonlinear partial differential equations. *Journal of Computational physics*, 378:686–707, 2019.

[53] Yann LeCun. The mnist database of handwritten digits. <http://yann.lecun.com/exdb/mnist/>, 1998.

[54] Karen Simonyan and Andrew Zisserman. Very deep convolutional networks for large-scale image recognition. In *International Conference on Learning Representations*, 2015.

[55] Alex Krizhevsky, Geoffrey Hinton, et al. Learning multiple layers of features from tiny images. *Toronto, ON, Canada*, 2009.

[56] Diederik P. Kingma and Jimmy Ba. Adam: A method for stochastic optimization, 2017. URL <https://arxiv.org/abs/1412.6980>.

[57] Kaiming He, Xiangyu Zhang, Shaoqing Ren, and Jian Sun. Deep residual learning for image recognition. In *Proceedings of the IEEE Conference on Computer Vision and Pattern Recognition (CVPR)*, June 2016.

[58] Ya Le and Xuan S. Yang. Tiny imagenet visual recognition challenge. CS231N, 2015.

[59] Alexey Dosovitskiy, Lucas Beyer, Alexander Kolesnikov, Dirk Weissenborn, Xiaohua Zhai, Thomas Unterthiner, Mostafa Dehghani, Matthias Minderer, Georg Heigold, Sylvain Gelly, Jakob Uszkoreit, and Neil Houlsby. An image is worth 16x16 words: Transformers for image recognition at scale. In *International Conference on Learning Representations*, 2021. URL <https://openreview.net/forum?id=YicbFdNTTy>.

[60] Olga Russakovsky, Jia Deng, Hao Su, Jonathan Krause, Sanjeev Satheesh, Sean Ma, Zhiheng Huang, Andrej Karpathy, Aditya Khosla, Michael Bernstein, Alexander C. Berg, and Li Fei-Fei. Imagenet large scale visual recognition challenge. *International Journal of Computer Vision*, 115(3):211–252, 2015. doi: 10.1007/s11263-015-0816-y. URL <https://doi.org/10.1007/s11263-015-0816-y>.

[61] Karel Lenc and Andrea Vedaldi. Understanding image representations by measuring their equivariance and equivalence. In *Proceedings of the IEEE Conference on Computer Vision and Pattern Recognition (CVPR)*, June 2015.

[62] Chiyuan Zhang, Samy Bengio, Moritz Hardt, Benjamin Recht, and Oriol Vinyals. Understanding deep learning (still) requires rethinking generalization. *Commun. ACM*, 64(3):107–115, feb 2021. ISSN 0001-0782. doi: 10.1145/3446776. URL <https://doi.org/10.1145/3446776>.

[63] Ronen Eldan and Ohad Shamir. The power of depth for feedforward neural networks. In Vitaly Feldman, Alexander Rakhlin, and Ohad Shamir, editors, *29th Annual Conference on Learning Theory*, volume 49 of *Proceedings of Machine Learning Research*, pages 907–940, Columbia University, New York, New York, USA, 23–26 Jun 2016. PMLR. URL <https://proceedings.mlr.press/v49/eldan16.html>.

[64] David Balduzzi, Marcus Frean, Lennox Leary, J. P. Lewis, Kurt Wan-Duo Ma, and Brian McWilliams. The shattered gradients problem: If resnets are the answer, then what is the question? In Doina Precup and Yee Whye Teh, editors, *Proceedings of the 34th International Conference on Machine Learning*, volume 70 of *Proceedings of Machine Learning Research*, pages 342–350. PMLR, 06–11 Aug 2017. URL <https://proceedings.mlr.press/v70/balduzzi17b.html>.

[65] Alec Radford, Jong Wook Kim, Chris Hallacy, Aditya Ramesh, Gabriel Goh, Sandhini Agarwal, Girish Sastry, Amanda Askell, Pamela Mishkin, Jack Clark, Gretchen Krueger, and Ilya Sutskever. Learning transferable visual models from natural language supervision. In Marina Meila and Tong Zhang, editors, *Proceedings of the 38th International Conference on Machine Learning*, volume 139 of *Proceedings of Machine Learning Research*, pages 8748–8763. PMLR, 18–24 Jul 2021. URL <https://proceedings.mlr.press/v139/radford21a.html>.

[66] Frederik Pahde, Maximilian Dreyer, Moritz Weckbecker, Leander Weber, Christopher J. Anders, Thomas Wiegand, Wojciech Samek, and Sebastian Lapuschkin. Navigating neural space: Revisiting concept activation vectors to overcome directional divergence. In *The Thirteenth International Conference on Learning Representations*, 2025. URL <https://openreview.net/forum?id=Q95MaWfF4e>.

[67] Sebastian Bach, Alexander Binder, Grégoire Montavon, Frederick Klauschen, Klaus-Robert Müller, and Wojciech Samek. On pixel-wise explanations for non-linear classifier decisions by layer-wise relevance propagation. *PLOS ONE*, 10(7):1–46, 07 2015. doi: 10.1371/journal.pone.0130140. URL <https://doi.org/10.1371/journal.pone.0130140>.

[68] Tolga Bolukbasi, Adam Pearce, Ann Yuan, Andy Coenen, Emily Reif, Fernanda Viégas, and Martin Wattenberg. An interpretability illusion for bert, 2021. URL <https://arxiv.org/abs/2104.07143>.

[69] Zhou Wang, A.C. Bovik, H.R. Sheikh, and E.P. Simoncelli. Image quality assessment: from error visibility to structural similarity. *IEEE Transactions on Image Processing*, 13(4):600–612, 2004. doi: 10.1109/TIP.2003.819861.

[70] Richard Zhang, Phillip Isola, Alexei A. Efros, Eli Shechtman, and Oliver Wang. The unreasonable effectiveness of deep features as a perceptual metric. In *Proceedings of the IEEE Conference on Computer Vision and Pattern Recognition (CVPR)*, June 2018.

[71] Alex Krizhevsky, Ilya Sutskever, and Geoffrey E Hinton. Imagenet classification with deep convolutional neural networks. In *Advances in Neural Information Processing Systems*, volume 25, 2012. URL https://proceedings.neurips.cc/paper_files/paper/2012/file/c399862d3b9d6b76c8436e924a68c45b-Paper.pdf.

[72] OpenAI. Clip: Connecting text and images. <https://github.com/openai/CLIP>, 2021.

[73] Snehil Sanyal. Weapon Detection Test. Kaggle dataset, 2023. Available at <https://www.kaggle.com/datasets/snehilsanyal/weapon-detection-test>.

[74] Ilya Loshchilov and Frank Hutter. Decoupled weight decay regularization. In *International Conference on Learning Representations*, 2019. URL <https://openreview.net/forum?id=Bkg6R1CqY7>.

- [75] Sébastien Marcel and Yann Rodriguez. Torchvision the machine-vision package of torch. In *Proceedings of the 18th ACM international conference on Multimedia*, pages 1485–1488, 2010.
- [76] Mayukh Deb. Feature visualization library for pytorch. <https://github.com/Mayukhdeb/torch-dreams>, 2021.
- [77] Tensorflow. lucid. <https://github.com/tensorflow/lucid>, 2017.
- [78] Haohan Wang, Songwei Ge, Zachary Lipton, and Eric P Xing. Learning robust global representations by penalizing local predictive power. In H. Wallach, H. Larochelle, A. Beygelzimer, F. d'Alché-Buc, E. Fox, and R. Garnett, editors, *Advances in Neural Information Processing Systems*, volume 32. Curran Associates, Inc., 2019. URL https://proceedings.neurips.cc/paper_files/paper/2019/file/3eefceb8087e964f89c2d59e8a249915-Paper.pdf.

A Related Work on Feature Visualization Manipulation

In this section we provide a more detailed description of the various attacks on Feature Visualization (FV) from Sec. 2.2, as well as methodological comparison to *Gradient Slingshots*.

Fooling Circuits The first attack scheme proposed by Geirhos et al. [38] introduces a *fooling circuit*: a module consisting of six interconnected units (see Fig. 8), where each one of them has a dedicated function. It is designed to route natural and synthetic inputs generated throughout the FV optimization procedure along separate computational paths. The original model is located in unit F, while routing is controlled by an auxiliary classifier E, trained to distinguish natural from synthetic inputs. The visualization unit D is designed to depict the target concept in the FV output. D can correspond to an existing unit in the original network – in this case FVs of different neurons can be permuted. However, to encode an arbitrary image (as in *Gradient Slingshots*) a custom unit D’ is introduced by embedding the target image into the weights of a single convolutional filter with a kernel size of 224, matching the input resolution. Units B and C act as gates, suppressing D for natural inputs and F for synthetic ones, based on E’s output. Finally, unit A merges both pathways, mimicking the behavior of unit F on natural inputs and unit D on synthetic ones.

Silent Units The second attack method proposed by Geirhos et al. [38] leverages *silent units*—units that remain inactive for all inputs in the training set but become strongly activated by FV signals. The authors modify an intermediate layer of a ResNet-50 by replacing a standard convolution-based computational block y with a manipulated block $\bar{y} = y + \Delta y$, where the added term Δy is constructed to be zero (or near zero) for natural images but dominates the output \bar{y} during FV optimization. This is done by adding an orthogonal perturbation to the original convolutional filters along with a negative bias calibrated to suppress activation on natural inputs. The method relies on the empirical observation that FVs typically produce stronger activations than natural images, allowing the manipulated units to dominate the FV outputs without affecting the network’s normal inference behavior. Although the authors state the method is architecture-agnostic, their experiments and description are limited to specific convolutional blocks. In comparison, we demonstrate the efficacy of *Gradient Slingshots* on both CNNs and vision transformers (ViTs).

While the work by Geirhos et al. [38] provides the first viable proof-of-concept that FVs can be arbitrarily manipulated, both the *fooling circuit* and *silent units* approaches rely on architectural modifications. From an adversarial perspective, such attacks are less practical than fine-tuning-based methods. Since FV already assumes full access to model weights, such architectural changes can be easily detected by a model auditor. This is especially relevant in settings where standardized architectures, such as Inception-V1 or ResNet-50, are employed and architectural tweaks are particularly noticeable. Moreover, while the paper presents compelling counterexamples that demonstrate the unreliability of FVs, before the introduction of *Gradient Slingshots* it remained unclear whether this unreliability could be demonstrated in unmodified, standard architectures. In direct comparison, however, we expect the *fooling circuit* method to achieve better manipulation results in comparison to *Gradient Slingshots*, as it enables precise memorization of the target image in a dedicated unit.

Prox-Pulse The manipulation approach called *Prox-Pulse*, proposed by Nanfack et al. [49], relies on fine-tuning rather than architectural changes, similar to our *Gradient Slingshots* method. Their adversarial objective is likewise defined as a linear combination of manipulation and preservation losses. The manipulation loss encourages high activations within a ρ -ball around the target image by “pushing up” the lowest activations in that region. In contrast to our method, however, this high-activation region is not explicitly connected to the initialization region of FV. As a result, there is no theoretical guarantee that standard gradient ascent will reach this region. The preservation loss is defined as the cross-entropy between the outputs of the original and manipulated models, and does not explicitly control for preservation of model internal activations. It therefore remains

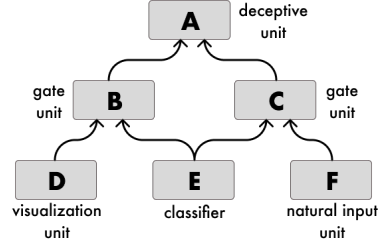


Figure 8: *Fooling circuit* for manipulation of FV. The original model (unit F) is embedded in a circuit such that the circuit output A activates as F on natural images, but as a unit with a desired FV on synthetic images. Adapted from Fig. 3 in [38].

unclear whether *Prox-Pulse* alters the model’s internal representations or merely its explanations. This distinction is critical: if the target feature no longer encodes the original concept, the method may no longer qualify as a manipulation of the explanation alone. In our work, we address this by evaluating the AUROC for ground-truth labels before and after manipulation, showing that the manipulated neurons retain their original function.

B Target Image Memorization in Gradient Slingshots

The *Gradient Slingshots* method fine-tunes a model such that the FV output of a target feature yields an image resembling an arbitrary target. Intuitively, this requires the model to be able to “memorize” the target – i.e., to distinguish it from all other points in the input space. In CNNs, convolutional filters act as an information bottleneck: they are trained to recognize specific patterns and discard irrelevant features. While, in principle, a single convolutional filter with the same spatial resolution as the input could directly encode the target (as implemented by Geirhos et al. [38]), practical CNN architectures impose constraints through limited filter size and count, as well as pooling operations.

Therefore, we hypothesize that the CNN’s ability to align the FV of its feature with the target should improve as the number and the spatial resolution of these filters increase relative to the model input dimensions. Empirically, we support this hypothesis by demonstrating in Sec. 4 that on lower-dimensional datasets such as MNIST and CIFAR-10 – where the input filter resolution and count are large relative to the input dimensions (see Appendices C.4 and C.5) – the manipulation yields significantly better alignment with the target than on higher-dimensional datasets like ImageNet. Additionally, in Sec. 4.2, we show that increasing the CNN width, and consequently the number of channels per layer, further improves the similarity between the manipulated FV and the target.

Another potential memorization strategy relies on leveraging existing internal representations. Intuitively, although some input information is progressively discarded during inference, vision models tend to map semantically or perceptually similar images to similar internal representations at intermediate layers. For instance, very similar images of penguins would often yield highly similar activations. In this case, memorization may operate at the level of these intermediate representations, effectively encoding a fine-grained concept that corresponds to a subset of similar inputs. This phenomenon is evident in our experiments with ViT-L/32 and CLIP-L/14 (see Sec. 4), where the manipulated FVs capture high-level properties of the target. However, the resemblance is not exact: as shown in Fig. 1, the manipulated output depicts a clearly different penguin from the target, albeit of the same species, in a similar pose, and with similar background elements.

C Experimental Details

We provide additional experimental details for the illustrative toy example in Sec. 3.3, as well as for the evaluations in Secs. 4 to 6. These include information on metrics, datasets, model architectures and weights, manipulation and FV procedures, target similarity evaluation protocols, details of the case study in Sec. 5, and compute resources.

C.1 Toy Experiment

In this section, we describe the experimental details related to experiments from Sec. 3.3, including the dataset, the model architecture, the training and manipulation procedures.

Dataset Initially, a 2-dimensional classification problem was formulated by uniformly sampling 512 data points for the positive class within the two-dimensional ball $A^+ = \{\mathbf{q} : \|\mathbf{q}\| < 2, \mathbf{q} \in \mathbb{R}^2\}$, and the same number of points for the negative class from the disc $A^- = \{\mathbf{q} : 4 < \|\mathbf{q}\| < 5, \mathbf{q} \in \mathbb{R}^2\}$. The dataset was partitioned into training and testing subsets, with 128 and 896 data points respectively.

Model The MLP architecture is as follows: input (2 units) \rightarrow fully connected (100 units) $\times 5 \rightarrow$ softmax (2 units). A Tanh activation function was applied after each linear layer, except for the final layer. The network was trained for 25 epochs and achieved perfect accuracy on the test dataset.

Manipulation The *Gradient Slingshots* method was employed to manipulate the post-softmax neuron responsible for the score of the positive class. In the manipulation phase, the “slingshot” and

the “landing” zones were defined as follows:

$$\mathbb{B} = \{\mathbf{q} : \|\mathbf{q} - \tilde{\mathbf{q}}\|_2 < 4\}, \quad (13)$$

$$\mathbb{L} = \{\mathbf{q} : \|\mathbf{q} - \mathbf{q}^t\|_2 < 4\}, \quad (14)$$

where $\tilde{\mathbf{q}} = (15, -20)$, and $\mathbf{q}^t = (20, -10)$, and the “tunnel” $\mathbb{T}_{B,L}$ was constructed according to the Equation 6.

For the set \mathbb{U} (uniform samples from the “tunnel” $\mathbb{T}_{B,L}$), we generated a total of $N = 50000$ points. The set \mathbb{X} consisted of $|\mathbb{X}| = 15000$ points, with both coordinates independently sampled from a normal distribution $\mathcal{N}(0, 10)$. The parameter γ was set to 0.025.

C.2 Evaluation Metrics

To compare the FV output to the target images, four image similarity metrics, Mean Squared Error (MSE), the Structural Similarity Index (SSIM) [69], Learned Perceptual Image Patch Similarity (LPIPS) [70] and distance in CLIP [65] feature space, are employed. MSE serves as an error measure, with values close to 0 signifying a high degree of resemblance. SSIM, on the other hand, is a perceptual similarity metric ranging between 0 and 1, where a higher SSIM value indicates increased similarity between images, and a value of 1 denotes identical images. LPIPS is a perceptual distance measure, whereby a lower LPIPS score indicates a higher similarity between the two images. In our study, the LPIPS calculations rely on the deep embeddings extracted from an AlexNet model [71] that has been pre-trained on the ImageNet dataset [60]. For CLIP-based comparison, we compute the cosine similarity between the target and FV-generated images in the visual encoder space of CLIP ViT-B/16 (OpenAI weights [72]). Additionally, we use the Area Under the Receiver Operating Characteristic curve (AUROC) to assess how well a feature distinguishes images of its ground-truth label from others.

C.3 Experimental Settings

For brevity, each experimental setting is assigned a label, as listed in Table 4. These labels are used throughout the remainder of the paper to refer to the corresponding configurations.

Table 4: Labels for the experimental settings in Secs. 4 to 6.

Reference	Model	Setting
Introduction of Sec. 4	6-layer CNN	6-layer CNN
Introduction of Sec. 4	VGG-9 [54]	VGG-9
Sec. 4.2	Modified VGGs	VGGs-Size
Introduction of Secs. 4 and 4.3	ResNet-18 [57]	ResNet-18
Introduction of Sec. 4, Secs. 4.1 and 6	ResNet-50 [57]	ResNet-50
Introduction of Sec. 4	ViT-L/32	ViT-L/32 [59]
Fig. 1, Secs. 5 and 6,	CLIP ViT-L/14	CLIP ViT-L/14 [65]

C.4 Datasets

In Table 5, we provide train–test splits and preprocessing details for all experimental settings except **CLIP ViT-L/14**. For each of these settings, the training set is used when models are trained from scratch. A subset (or the entirety) of this training set is also used to compute the preservation loss (see Appendix C.6). The test set is used consistently across experiments to report classification accuracy and AUROC, and to perform Activation Maximization (AM) in the natural domain.

For training of the weapon detection head in the **CLIP ViT-L/14** setting, we used the Weapon Detection Dataset [73] for all weapon categories except “assault rifle”. We scraped 267 images of “assault rifles” from Wikimedia Commons¹, allocating 200 for training and adversarial fine-tuning, 40 for evaluation, and 27 for feature vector computation. We applied the same protocol for “gentoo

¹<https://commons.wikimedia.org/w/index.php?search=assault+rifles&title=Special:MediaSearch&type=image>

Table 5: Dataset details, train/test splits, image resolutions, and preprocessing steps used during training and/or *Gradient Slingshots* fine-tuning.

Setting	Dataset	Train-Test Split	Image Size	Train Preprocessing
6-layer CNN VGG-9 and VGGs-Size	MNIST [53] CIFAR-10 [55]	80% / 20% Default (80% / 20%)	28×28 32×32	Normalization only Resize to 32×32, random horizontal flip (p=0.5), 4px padding, random crop to 32×32, normalization
ResNet-18	TinyImageNet [58]	80% / 20% of train set	64×64	Resize to 64×64, random horizontal flip (p=0.5), 4px padding, random crop to 64×64, normalization
ResNet-50	ImageNet [60]	Default; val. used as test	224×224	Random resized crop to 224×224, random rotation (0–20°), horizontal flip (p=0.1), normalization
ViT-L/32	ImageNet	Default; val. used as test	224×224	Random resized crop to 224×224, random rotation (0–20°), horizontal flip (p=0.1), normalization

penguin" images², collecting 240 in total: 200 for training and adversarial fine-tuning, and 40 for evaluation. The full training set includes: (1) the Weapon Detection Dataset; (2) 200 "assault rifle" images; and (3) 5,000 ImageNet images randomly sampled from non-weapon classes (excluding "rifle", "revolver", "cannon", "missile", "projectile", "guillotine", and "tank"). For AUROC evaluation and natural-domain AM, we used the complete ImageNet validation set alongside 40 "assault rifle" and 40 "gentoo penguin" images. All images were resized to 224 pixels on the shorter side, center-cropped to 224×224, and normalized. Images shown in Fig. 7 are all from ImageNet.

C.5 Model Architecture and Training

The 6-layer CNN architecture is as follows: input -> conv (5x5, 16) -> max pooling (2x2)-> conv (5x5, 32) -> max pooling (2x2) -> fully connected (512 units) -> fully connected (256 units) -> fully connected (120 units) -> fully connected (84 units) -> softmax (10 units). ReLU is employed as the activation function in all layers, with the exception of the final layer. We trained the model with the SGD optimizer using learning rate of 0.001 and momentum of 0.9 until convergence. The final test set accuracy of this model is 99.87%.

The CNN architectures for **VGGs-Size** are detailed in Table 6. In **VGG-9**, the configuration A64 is used. Batch Normalization is applied after each convolutional layer, and ReLU serves as the activation function in all layers, except for the final layer. The convolutional layer stacks of models "A64", "B64", "C64", and "D64" align with those in the VGG11, VGG13, VGG16, and VGG19 architectures [54]. The original 16 models for CIFAR-10 were trained using AdamW [74] with a learning rate of 0.001 and weight decay of 0.01 until convergence. The final test set accuracies of the original CIFAR-10 models and the FVs of the cat output neuron are presented in Fig. 9.

In the **ResNet-18** setting, we adapted ResNet-18 for the lower-resolution inputs of the TinyImageNet dataset by replacing the initial 7×7 convolution and 3×3 max-pooling with a single 3×3 convolution (stride 1, padding 1). We trained the model with SGD with a learning rate 0.001 and momentum 0.9 for 30 epochs. The final test accuracy in this setting is 71.89%.

To construct the weapon-detection model in the **CLIP ViT-L/14** setting, we added a multilayer perceptron (MLP) on top of a frozen CLIP-L/14 visual encoder. The MLP architecture is as follows:

²<https://commons.wikimedia.org/w/index.php?search=Pygoscelis+papua&title=Special:MediaSearch&type=image>

Table 6: CIFAR-10 CNN configurations with added layers. The convolutional layer parameters are denoted as “conv⟨receptive field size⟩-⟨number of channels⟩”. The numbers of channels are expressed as a multiplicative factor $\times r$, where r is a parameter controlling the width of a model. The batch normalization layers and ReLU activation function are not shown for brevity. The model depth configurations are labeled from “A” to “D”.

Layers	A	B	C	D
input (32 × 32 RGB image)				
conv3-(1 × r)	✓	✓	✓	✓
conv3-(1 × r)		✓	✓	✓
maxpool				
conv3-(2 × r)	✓	✓	✓	✓
conv3-(2 × r)		✓	✓	✓
maxpool				
conv3-(4 × r)	✓	✓	✓	✓
conv3-(4 × r)	✓	✓	✓	✓
conv1-(4 × r)			✓	✓
conv3-(4 × r)				✓
maxpool				
conv3-(8 × r)	✓	✓	✓	✓
conv3-(8 × r)	✓	✓	✓	✓
conv1-(8 × r)			✓	✓
conv3-(8 × r)				✓
maxpool				
conv3-(8 × r)	✓	✓	✓	✓
conv3-(8 × r)	✓	✓	✓	✓
conv1-(8 × r)			✓	✓
conv3-(8 × r)				✓
maxpool				
FC-8 × r				
Dropout(0.5)				
FC-10				

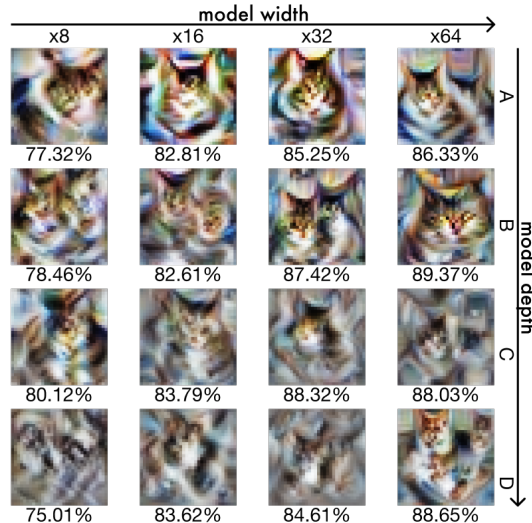


Figure 9: 16 classification models of varying depth (“A” - “D”) and width ($\times 8$ - $\times 64$) trained on CIFAR-10 were manipulated to change the FV of the cat output neuron to a fish image. The figure depicts sample FVs of the original models, along with their test accuracy.

Table 7: Weights specification and sources of the pretrained models.

Model	Pretrained Weights Source
ResNet-50	Torchvision ResNet50_Weights. IMAGENET1K_V1 [75]
ViT-L/32	Torchvision ViT_L_32_Weights. IMAGENET1K_V1 [75]
CLIP ViT-L/14	OpenAI CLIP ViT-L/14 [72]

input \rightarrow fully connected (512 units) \rightarrow ReLU \rightarrow output (1 unit). We trained the MLP optimizing with Adam (learning rate $1e-4$, batch size 32) for 5 epochs.

The sources for the weights of models that we did not train from scratch are provided in Table 7.

C.6 Gradient Slingshots Fine-Tuning Procedures

Manipulation Sets For the **6-layer CNN**, we targeted Pixel-AM, with the manipulation set sampled directly in the input (pixel) domain. In all other settings, manipulations were targeting Fourier FV, so the manipulation set was sampled in the frequency domain. Prior to being fed into the models, these frequency-domain points were processed by scaling, applying an inverse 2D real Fast-Fourier Transform (FFT), converting from the custom colorspace to RGB, and finally applying a sigmoid function to map values to the $[0,1]$ range for visualization, following implementations from the `lucid` and `torch-dreams` libraries [76]. The radii of the slingshot σ_B and landing zones σ_L are provided in Table 9. At each fine-tuning step, a number of points equal to the batch size (see Table 10) are sampled uniformly from the tunnel region defined in Eq. (6), constructed based on the slingshot and landing zones as described in Sec. 3.1.

Preservation Sets In Table 8, we provide details on the construction of datasets used for the calculation of the preservation loss Eq. (11). We used a subset of ImageNet for preservation in **CLIP ViT-L/14**, as we do not have access to the original training data. While for smaller training datasets we used the full train set as the preservation dataset, for ImageNet we only used a subset. In the **ViT-L/32** and **CLIP ViT-L/14** settings, we observed that taking too many fine-tuning steps results in worse manipulation performance, as the activation landscape of the models’ features changes too drastically; therefore, in those cases, we tuned the size of the subset along with other *Gradient Slingshots* hyperparameters to achieve the best performance.

Table 8: Composition of the datasets used to compute the preservation loss (Eq. (11)) during *Gradient Slingshots* fine-tuning.

Setting	Preservation Set
6-layer CNN	The full train set.
VGG-9	The full train set.
VGGs-Size	The full train set.
ResNet-18	The full train set.
ResNet-50	Subset of 64 classes in the train set (ImageNet), including “Dalmatian”, “wolf spider.”
ViT-L/32	10% of “sealion” and “broccoli” classes and 0.12% of samples of other classes in the train set (ImageNet).
CLIP ViT-L/14	0.28% of ImageNet + 200 images scraped from Wikimedia Commons under categories “Assault rifles” and “Pygoscelis papua” each.

Hyperparameters of Gradient Slingshots Table 9 summarizes the hyperparameters and specifications of the *Gradient Slingshots* attack. In all settings, we used $\tilde{q} = 0.0$, as it is standard practice for the initialization distribution I to be normal with zero mean [77]. As discussed in Sec. 7, hyperparameter tuning is computationally intensive. The remaining parameters were selected by evaluating a range of configurations, each run for 1–3 epochs and assessed both qualitatively (via visualization of manipulated feature vectors) and quantitatively (via changes in classification accuracy). Once a satisfactory configuration was identified, we performed a sweep over nearby values of α to generate the evaluation results reported in Sec. 4.1 and Appendix D.1.

Table 9: *Gradient Slingshots* method hyperparameters and specifications: α from Eq. (12), w from Eq. (11), γ from Eq. (9), constant C for Eq. (10), the radius of the slingshot zone” σ_B and the landing zone” σ_L used to define the sampling “tunnel” in Eq. (6), and the choice of manipulation loss— $\mathcal{L}_{\mathcal{M}}^{\text{act?}}$ = True indicates that the activation-based manipulation loss (Eq. (10)) was used instead of the gradient-based loss (Eq. (9)).

Setting	α	w	γ	C	σ_B	σ_L	$\mathcal{L}_{\mathcal{M}}^{\text{act?}}$
6-layer CNN	0.8	0	10	NA	0.1	0.1	False
VGG-9	0.025	0	10	NA	0.1	0.1	False
VGGs-Size		0.01	0.1	10	NA	0.1	0.1
ResNet-18	0.995	0.01	1000	NA	0.01	0.01	False
ResNet-50	0.64	0.01	200	NA	0.01	0.01	False
ViT-L/32	0.9995	0.01	100	1	0.01	0.01	True
CLIP ViT-L/14	0.99991	1	2000	1	0.01	0.01	True

Fine-tuning specifications are provided in Table 9. All models were fine-tuned using the AdamW optimizer with the listed learning rate (LR), weight decay and a numerical stability constant ϵ^{ADAM} (corresponding to ϵ in Algorithm 2 of [74]). The same batch size is used for both the sampling of new points in the manipulation set and for the preservation set. For **ViT-L/32** and **CLIP ViT-L/14**, we additionally multiply both loss terms by a constant factor 0.0001, for numerical stability.

Table 10: Training and optimization parameters for *Gradient Slingshots* fine-tuning. “Weight Decay” and ϵ^{ADAM} refer to the corresponding parameters of the Adam optimizer.

Setting	Epochs	LR	Weight Decay	ϵ^{ADAM}	Batch Size
VGG-9	50	0.0001	0.001	1e-08	32
VGGs-Size	100	0.001	0.001	1e-08	32
6-layer CNN	30	0.001	0.001	1e-08	32
ResNet-18	5	1e-05	0.001	1e-08	64
ResNet-50	10	1e-06	0.001	1e-08	32
ViT-L/32	1	0.0002	0.05	1e-07	16
CLIP ViT-L/14	1	2e-06	0.01	1e-07	8

Target Images The target images and their sources are listed in Table 11. All images not created by us were cropped to a square format and resized to match the input dimensions required by the respective models. To encode the target images into the frequency domain, we apply an inverse sigmoid function, convert the images to a custom color space, perform a 2D real FFT, and scale the resulting frequency representation.

C.7 Feature Visualization Procedures

In Table 12, we specify the parameters of the FV, including the initialization parameters, the FV step size, the number of FV optimization steps, as well as the regularization strategy. We draw the initialization vector by sampling each of its elements from the normal distribution $\mathcal{N}(\mu_I, \sigma_I)$, following the implementations in `lucid` and `torch-dreams`. For pixel-AM, the initialization signal is in the input domain. For FV, the initialization signal is sampled in the scaled frequency domain and transformed into the pixel domain employing the scaled FFT function, as described in Appendix C.6. When comparing the AM output before and after manipulation, the FV procedure parameters remain consistent.

The following defines the abbreviations used for optimization and regularization techniques under the “FV Strategy” column in Table 12:

Gradient clipping (GC) Gradient clipping is a method employed to mitigate the issue of exploding gradients, typically observed in DNNs. This method is also being used in the scope of synthetic FV. We constrain the gradient norm to 1.0.

Table 11: Target images, their sources, and licensing attributions where applicable.

Setting	Target image	Displayed in	Source / License
VGG-9	“FAKE”	Fig. 3	Created by us
VGGs-Size	“fish”	Fig. 5	ImageNet [60]
6-layer CNN	“cross”	Fig. 3	Created by us
ResNet-18	“harvester”	Fig. 3	ImageNet
	“grey”	Fig. 6 (A)	Created by us
	“pink”	Fig. 6 (B)	Created by us
	“dog sketch”	Fig. 6 (C)	ImageNet-Sketch [78]
	“tiger”	Fig. 6 (D)	TinyImageNet [58]
	“nail”	Fig. 6 (E)	TinyImageNet
	“lion”	Fig. 6 (F)	TinyImageNet
	“basketball”	Fig. 6 (G)	ImageNet
	“bird in water”	Fig. 6 (H)	ImageNet
	“bird on a branch”	Fig. 6 (I)	ImageNet
	“cacadoo”	Fig. 6 (J)	ImageNet
	“spider”	Fig. 14 (K)	TinyImageNet
	“python”	Fig. 14 (L)	ImageNet
	“puppy”	Fig. 14 (M)	TinyImageNet
ResNet-50	“Dalmatian”	Fig. 3	Photo by Maja Dumat / CC BY 2.0
ViT-L/32	“sealions”	Fig. 3	Photo by William Warby / CC BY 2.0
CLIP ViT-L/14	“gentoo penguin”	Fig. 1	Photo by William Warby / CC BY 2.0

Table 12: Specifications of FV procedures. μ_I and σ_I denote the mean and standard deviation of the FV initialization distribution. “FV Strategies” refers to the optimization and regularization recipe used.

Setting	μ_I	σ_I	Step Size	Steps	FV Strategies
6-layer CNN	0.0	0.01	0.1	200	None
VGG-9	0.0	0.01	1	100	GC
VGGs-Size	0.0	0.01	0.1	700	GC
ResNet-18	0.0	0.01	0.01	200	Adam + GC + TR
ResNet-50	0.0	0.01	0.01	500	Adam + GC + TR
ViT-L/32	0.0	0.01	0.003	2000	Adam + GC + TR
CLIP ViT-L/14	0.0	0.01	0.002	3000	Adam + GC + TR

Transformation robustness (TR) Transformation robustness has been introduced as a technique aimed at enhancing the interpretability of FVs. This technique is realized through the application of random perturbations to the signal at each optimization step and facilitates finding signals that induce heightened activation even when slightly transformed [32, 50].

For **ResNet-18** and **ResNet-50**, we apply the following sequence of transformations:

- padding the image by 2 pixels on all sides using a constant fill value of 0.5;
- random affine transformation with rotation degrees sampled from -20° to 20° , scaling factors from 0.75 to 1.025, and fill value 0.5;
- random crop to the target input resolution (224 x 224), with padding as needed (fill value 0.0).

For ViT-based settings **ViT-L/32** and **CLIP ViT-L/14**, we adapt the transformation robustness strategy to better align with the architectural characteristics of the models. The following sequence of transformations is applied during FV optimization:

- padding the image by 16 pixels on all sides using a constant fill value of 0.0;
- random affine transformation with rotation degrees sampled from the range -20° to 20° , scaling factors from 0.75 to 1.05, and a constant fill value of 0.0;

- another random rotation in the range -20° to 20° with fill value 0.0;
- addition of Gaussian noise with mean 0.0 and standard deviation 0.1;
- random resized crop back to the original model input resolution (224 x 224), with fixed aspect ratio and scale sampled from the range (0.5, 0.75).

The transformation sequences were selected through empirical experimentation with various recipes, drawing inspiration from Fel et al. [33], Tensorflow [77]. All transformations are implemented using the `torchvision` library.

Adam Adam [56], a popular optimization algorithm for training neural network weights, can also be applied in FV settings.

C.8 Evaluation Procedure for Target Similarity

For each evaluation model, we generated 100 samples of FV outputs, with the exception of **CLIP ViT-L/14**, for which only 30 samples were computed due to computational constraints. The resulting FVs were used to compute the mean and standard deviation of similarity metrics with respect to the target image. Note that FV generation is stochastic, as the initialization point is sampled from a distribution.

C.9 Application

For the experiments in the **CLIP-L/14** setting, we computed the “assault rifle” feature vector in the residual stream of layer 22 in the visual module of CLIP-L/14. We followed the Pattern-CAV approach [66]: we took the difference between the mean activations of 27 “assault rifle” images and the mean activations of 500 randomly sampled ImageNet images. The “assault rifle” images here were handpicked to have the concept be very present and recognizable in them.

C.10 Compute Resources

All experiments were conducted using a workstation with 2×24 GB NVIDIA® RTX 4090 GPUs and a compute cluster with 4×40 GB NVIDIA® A100 GPUs. Each experiment was performed on a single GPU. The approximate time required to compute Gradient Slingshot (GS) manipulation for each setting is as follows:

- **6-layer CNN**: 1 hour
- **VGG-9**: 2 hours
- **VGGs-Size**: 2–5 hours
- **ResNet-18**: 1 hour
- **ResNet-50**: 3 hours
- **ViT-L/32**: 1 minute
- **CLIP ViT-L/14**: 5 minutes

Overall, activation-based manipulation (Eq. (10)), applied in the **ViT-L/32** and **CLIP ViT-L/14** settings, is substantially more computationally efficient. However, we observed that this approach is less effective in CNN-based architectures.

Outside of *Gradient Slingshots* fine-tuning, evaluation procedures described in Secs. 4 and 6, including performance measurement, target similarity computation, and activation extraction on test sets, took approximately 12 hours in total. The experiments presented in Sec. 5 required around 2 hours of computations.

D Additional Experiments

D.1 Accuracy – Manipulation Trade-Off

We expand on the experimental results of the accuracy–manipulation trade-off analysis for the *Gradient Slingshots* attack, introduced in Sec. 4.1, with additional findings reported in Tables 13 to 16 and Figs. 10 to 13

Table 13: Accuracy–manipulation trade-off for the *Gradient Slingshots* attack on the “zero” output neuron in **6-layer CNN**. Reported are test accuracy (in %), AUROC for the “zero” class, and the mean \pm standard deviation of similarity metrics between the manipulated FV and the target image.

α	Acc.	AUROC	CLIP \uparrow	MSE \downarrow	LPIPS \downarrow	SSIM \uparrow
Original	99.67	1.00	0.88 \pm 0.01	0.13 \pm 0.01	0.15 \pm 0.01	0.04 \pm 0.03
0.900000	99.28	1.00	0.89 \pm 0.01	0.10 \pm 0.00	0.15 \pm 0.01	0.13 \pm 0.02
0.800000	98.98	1.00	0.93 \pm 0.01	0.03 \pm 0.00	0.11 \pm 0.02	0.74 \pm 0.01
0.700000	98.89	1.00	0.95 \pm 0.01	0.02 \pm 0.00	0.07 \pm 0.02	0.76 \pm 0.03
0.500000	98.10	1.00	0.86 \pm 0.01	0.12 \pm 0.00	0.29 \pm 0.04	0.07 \pm 0.02
0.200000	96.34	0.99	0.93 \pm 0.04	0.04 \pm 0.04	0.11 \pm 0.10	0.63 \pm 0.28
0.050000	94.36	0.99	0.86 \pm 0.01	0.11 \pm 0.00	0.24 \pm 0.01	0.15 \pm 0.01
0.010000	70.88	0.87	0.95 \pm 0.00	0.02 \pm 0.00	0.04 \pm 0.00	0.84 \pm 0.01
0.005000	52.52	0.84	0.96 \pm 0.01	0.02 \pm 0.00	0.03 \pm 0.00	0.82 \pm 0.01
0.001000	19.39	0.54	0.95 \pm 0.00	0.02 \pm 0.00	0.04 \pm 0.00	0.77 \pm 0.01

Table 14: Accuracy–manipulation trade-off for the *Gradient Slingshots* attack on the “cat” output neuron in **VGG9**. Reported are test accuracy (in %), AUROC for the “cat” class, and the mean \pm standard deviation of similarity metrics between the manipulated FV and the target image.

α	Acc.	AUROC	CLIP \uparrow	MSE \downarrow	LPIPS \downarrow	SSIM \uparrow
Original	86.33	0.97	0.74 \pm 0.02	0.07 \pm 0.01	0.25 \pm 0.02	0.03 \pm 0.02
0.9900	86.10	0.97	0.74 \pm 0.02	0.08 \pm 0.01	0.25 \pm 0.02	0.03 \pm 0.02
0.8000	87.20	0.97	0.73 \pm 0.02	0.09 \pm 0.01	0.25 \pm 0.02	0.03 \pm 0.02
0.5000	83.90	0.97	0.78 \pm 0.02	0.01 \pm 0.00	0.09 \pm 0.01	0.20 \pm 0.05
0.1000	86.40	0.97	0.76 \pm 0.02	0.01 \pm 0.00	0.15 \pm 0.02	0.24 \pm 0.04
0.0500	85.10	0.96	0.75 \pm 0.02	0.02 \pm 0.00	0.11 \pm 0.02	0.25 \pm 0.04
0.0250	85.15	0.96	0.79 \pm 0.01	0.02 \pm 0.00	0.16 \pm 0.02	0.33 \pm 0.04
0.0100	81.90	0.95	0.81 \pm 0.02	0.01 \pm 0.00	0.14 \pm 0.03	0.41 \pm 0.05
0.0050	82.20	0.94	0.88 \pm 0.04	0.01 \pm 0.00	0.08 \pm 0.02	0.52 \pm 0.05
0.0010	72.70	0.86	0.87 \pm 0.04	0.01 \pm 0.00	0.09 \pm 0.02	0.54 \pm 0.04
0.0001	9.50	0.54	0.81 \pm 0.02	0.02 \pm 0.00	0.14 \pm 0.02	0.31 \pm 0.07

Table 15: Accuracy–manipulation trade-off for the *Gradient Slingshots* attack on the “gondola” output neuron in **ResNet-18**. Reported are test accuracy (in %), AUROC for the “gondola” class, and the mean \pm standard deviation of similarity metrics between the manipulated FV and the target image.

α	Acc.	AUROC	CLIP \uparrow	MSE \downarrow	LPIPS \downarrow	SSIM \uparrow
Original	71.89	0.99	0.64 \pm 0.03	0.09 \pm 0.01	0.60 \pm 0.04	0.04 \pm 0.02
0.997	69.50	0.97	0.73 \pm 0.03	0.07 \pm 0.01	0.34 \pm 0.04	0.06 \pm 0.03
0.995	71.40	0.97	0.75 \pm 0.03	0.07 \pm 0.01	0.34 \pm 0.06	0.07 \pm 0.03
0.993	68.40	0.96	0.73 \pm 0.03	0.07 \pm 0.01	0.40 \pm 0.06	0.07 \pm 0.03
0.990	69.30	0.94	0.73 \pm 0.03	0.07 \pm 0.01	0.42 \pm 0.05	0.07 \pm 0.03
0.950	39.10	0.87	0.69 \pm 0.03	0.10 \pm 0.01	0.58 \pm 0.04	0.04 \pm 0.02
0.900	11.00	0.79	0.70 \pm 0.02	0.08 \pm 0.01	0.57 \pm 0.04	0.08 \pm 0.03
0.500	0.60	0.63	0.62 \pm 0.03	0.15 \pm 0.01	0.51 \pm 0.03	0.03 \pm 0.02
0.100	0.80	0.51	0.67 \pm 0.04	0.10 \pm 0.04	0.61 \pm 0.14	0.10 \pm 0.02

Table 16: Accuracy–manipulation trade-off for the *Gradient Slingshots* attack on the “broccoli” output neuron in **ViT-L/32**. Reported are test accuracy (in %), AUROC for the “broccoli” class, and the mean \pm standard deviation of similarity metrics between the manipulated FV and the target image.

	α	Acc.	AUROC	CLIP \uparrow	MSE \downarrow	LPIPS \downarrow	SSIM \uparrow
Original		76.97	1.00	0.52 ± 0.02	0.08 ± 0.00	0.74 ± 0.02	0.08 ± 0.01
0.999999		76.58	1.00	0.51 ± 0.02	0.08 ± 0.00	0.75 ± 0.03	0.07 ± 0.01
0.999900		76.64	1.00	0.52 ± 0.03	0.09 ± 0.00	0.76 ± 0.03	0.07 ± 0.01
0.999500		76.06	0.99	0.50 ± 0.02	0.07 ± 0.00	0.77 ± 0.03	0.08 ± 0.01
0.999000		75.96	0.99	0.49 ± 0.02	0.07 ± 0.00	0.74 ± 0.02	0.09 ± 0.01
0.990000		72.42	0.99	0.49 ± 0.02	0.06 ± 0.00	0.73 ± 0.02	0.11 ± 0.01
0.100000		0.10	0.50	0.49 ± 0.02	0.05 ± 0.00	0.76 ± 0.02	0.18 ± 0.01

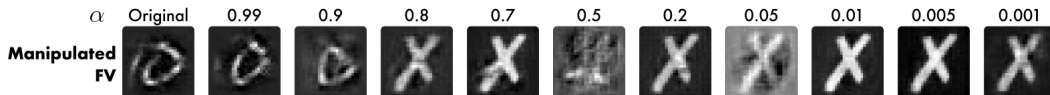


Figure 10: Sample FVs at different values of α for **6-layer CNN**.

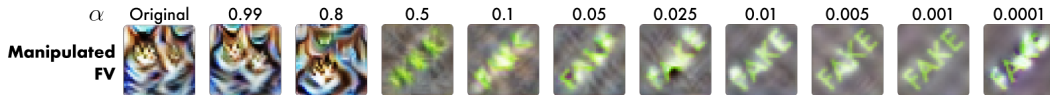


Figure 11: Sample FVs at different values of α for **VGG-9**.



Figure 12: Sample FVs at different values of α for **ResNet-18**.



Figure 13: Sample FVs at different values of α for **ViT-L/32**.

D.2 Impact of Target Image on Manipulation

We provide additional quantitative evaluation of the effect of the target image on manipulation success, extending the results from Appendix D.2 to an additional set of target images, shown in Fig. 14.

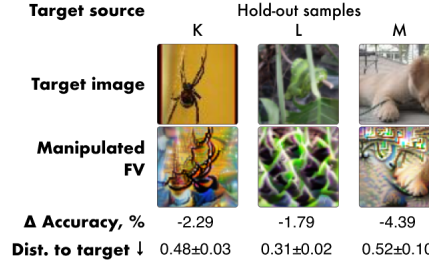


Figure 14: Manipulation results for different target images by source. Shown are example FV outputs, change in overall accuracy (p.p.), and mean \pm standard deviation of perceptual distance to the target (LPIPS). Manipulation is most effective with natural images.

D.3 Attack Detection

We provide additional qualitative results for our attack detection scheme in Fig. 15, extending the evaluation described in Sec. 6 to additional experimental settings.

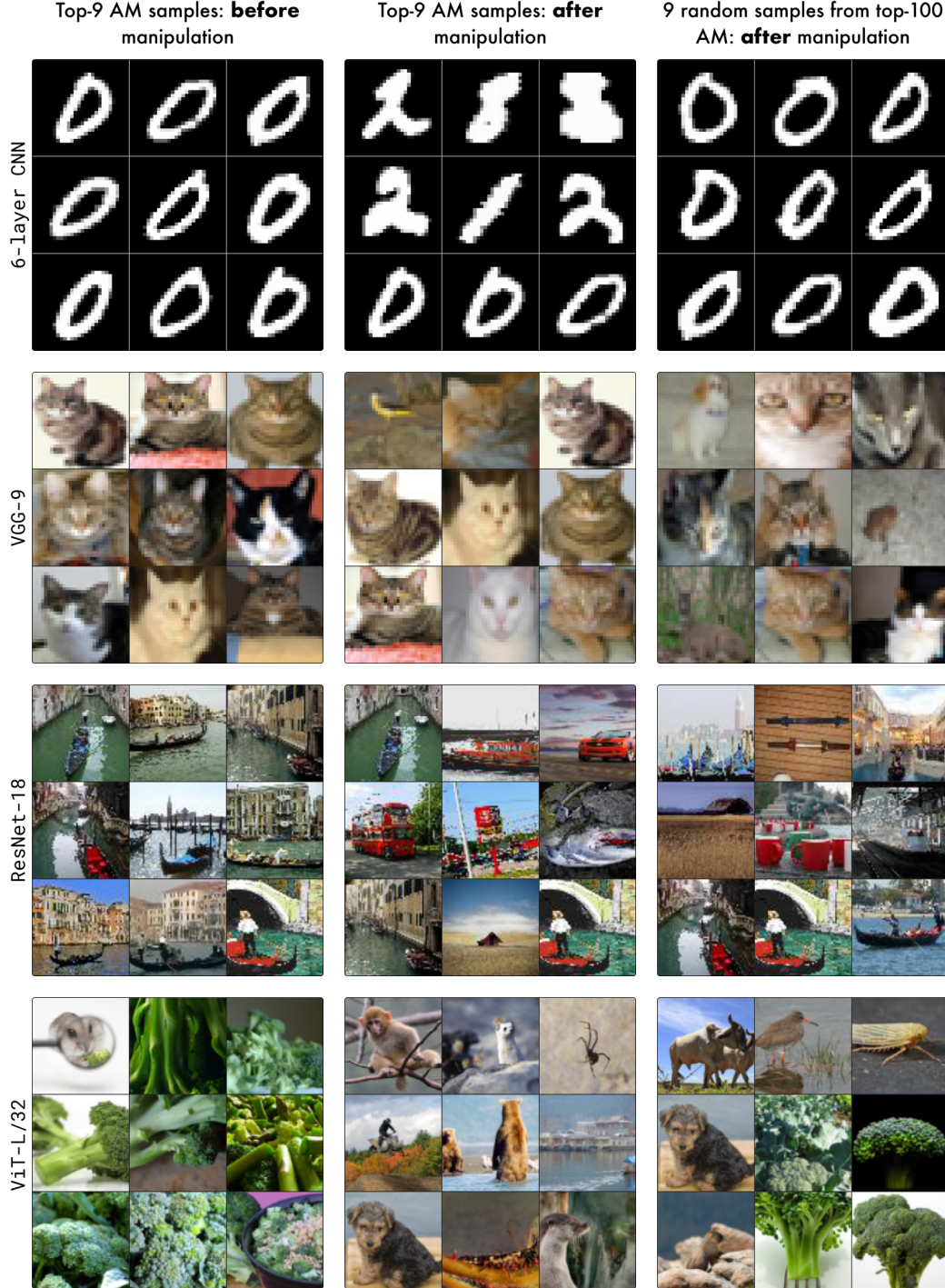


Figure 15: Top-9 most activating test samples before and after the *Gradient Slingshots* attack. While the attack can substantially change which samples rank as the most activating across a dataset, broader sampling from the top of the AM distribution often recovers the original concept.